







Search for Continuous and Transient Neutrino Emission Associated with IceCube's Highest-energy Tracks: An 11 yr Analysis

R. Abbasi¹, M. Ackermann², J. Adams³, S. K. Agarwalla^{4,64}, J. A. Aguilar⁵, M. Ahlers⁶, J. M. Alameddine⁷, N. M. Amin⁸, K. Andeen⁹, G. Anton¹⁰, C. Argüelles¹¹, Y. Ashida¹², S. Athanasiadou², S. N. Axani⁸, X. Bai¹³, A. Balagopal V.⁴, M. Baricevic⁴, S. W. Barwick¹⁴, V. Basu⁴, R. Bay¹⁵, J. J. Beatty^{16,17}, J. Becker Tjus^{18,65}, J. Beise¹⁹, C. Bellenghi²⁰, C. Benning²¹, S. BenZvi²², D. Berley²³, E. Bernardini²⁴, D. Z. Besson²⁵, E. Blaufuss²³, S. Blot², F. Bontempo²⁶, J. Y. Book¹¹, C. Boscolo Meneguolo²⁴, S. Böser²⁷, O. Botner¹⁹, J. Böttcher²¹, E. Bourbeau⁶, J. Braun⁴, B. Brinson²⁸, J. Brostean-Kaiser², R. T. Burley²⁹, R. S. Busse³⁰, D. Butterfield⁴, M. A. Campana³¹, K. Carloni¹¹, E. G. Carnie-Bronca²⁹, S. Chattopadhyay^{4,64}, N. Chau⁵, C. Chen²⁸, Z. Chen³², D. Chirkin⁴, S. Choi³³, B. A. Clark²³, S. Coenders²⁰, A. Coleman¹⁹, G. H. Collin³⁴, A. Connolly^{16,17}, J. M. Conrad³⁴, P. Coppin³⁵, P. Correa³⁵, D. F. Cowen^{36,37}, P. Dave²⁸, C. De Clercq³⁵, J. J. DeLaunay³⁸, D. Delgado¹¹, S. Deng²¹, K. Deoskar³⁹, A. Desai⁴, P. Desiati⁴, K. D. de Vries³⁵, G. de Wasseige⁴⁰, T. DeYoung⁴¹, A. Diaz³⁴, J. C. Díaz-Vélez⁴, M. Dittmer³⁰, A. Domi¹⁰, H. Dujmovic⁴, M. A. DuVernois⁴, T. Ehrhardt²⁷, A. Eimer¹⁰, P. Eller²⁰, E. Ellinger⁴², S. El Mentawi²¹, D. Elsässer⁷, R. Engel^{26,43}, H. Erpenbeck⁴, J. Evans²³, P. A. Evenson⁸, K. L. Fan²³, K. Fang⁴, K. Farrag⁴⁴, A. R. Fazely⁴⁵, A. Fedynitch⁴⁶, N. Feigl⁴⁷, S. Fiedlschuster¹⁰, C. Finley³⁹, L. Fischer², D. Fox³⁶, A. Franckowiak¹⁸, A. Fritz²⁷, P. Fürst²¹, J. Gallagher⁴⁸, E. Ganster²¹, A. Garcia¹¹, L. Gerhardt⁴⁹, A. Ghadimi³⁸, C. Glaser¹⁹, T. Glauch²⁰, T. Glüsenskamp^{10,19}, N. Goehke⁴³, J. G. Gonzalez⁸, S. Goswami³⁸, D. Grant⁴¹, S. J. Gray²³, O. Gries²¹, S. Griffin⁴, S. Griswold²², K. M. Groth⁶, C. Günther²¹, P. Gutjahr⁷, C. Haack¹⁰, A. Hallgren¹⁹, R. Halliday⁴¹, L. Halve²¹, F. Halzen⁴, H. Hamdaoui³², M. Ha Minh²⁰, K. Hanson⁴, J. Hardin³⁴, A. A. Harnisch⁴¹, P. Hatch⁵⁰, A. Haungs²⁶, K. Helbing⁴², J. Hellrung¹⁸, F. Henningsen²⁰, L. Heuermann²¹, N. Heyer¹⁹, S. Hickford⁴², A. Hidvegi³⁹, C. Hill⁴⁴, G. C. Hill²⁹, K. D. Hoffman²³, S. Hori⁴, K. Hoshina^{4,66}, W. Hou²⁶, T. Huber²⁶, K. Hultqvist³⁹, M. Hünnefeld⁷, R. Hussain⁴, K. Hymon⁷, S. In³³, A. Ishihara⁴⁴, M. Jacquart⁴, O. Janik²¹, M. Jansson³⁹, G. S. Japaridze⁵¹, M. Jeong¹², M. Jin¹¹, B. J. P. Jones⁵², N. Kamp¹¹, D. Kang²⁶, W. Kang³³, X. Kang³¹, A. Kappes³⁰, D. Kappesser²⁷, L. Kardum⁷, T. Karg², M. Karl²⁰, A. Karle⁴, A. Katil⁵³, U. Katz¹⁰, M. Kauer⁴, J. L. Kelley⁴, A. Khatee Zathul⁴, A. Kheirandish^{54,55}, J. Kiryluk³², S. R. Klein^{15,49}, A. Kochocki⁴¹, R. Koirala⁸, H. Kolanoski⁴⁷, T. Kontrimas²⁰, L. Köpke²⁷, C. Kopper¹⁰, D. J. Koskinen⁶, P. Koundal²⁶, M. Kovacevich³¹, M. Kowalski^{2,47}, T. Kozynets⁶, J. Krishnamoorthi^{4,64}, K. Kruiswijk⁴⁰, E. Krupczak⁴¹, A. Kumar², E. Kun¹⁸, N. Kurahashi³¹, N. Lad², C. Lagunas Gualda², M. Lamoureux⁴⁰, M. J. Larson²³, S. Latseva²¹, F. Lauber⁴², J. P. Lazar^{4,11}, J. W. Lee³³, K. Leonard DeHolton³⁷, A. Leszczyńska⁸, M. Lincetto¹⁸, Q. R. Liu⁴, M. Liubarska⁵³, E. Lohfink²⁷, C. Love³¹, C. J. Lozano Mariscal³⁰, L. Lu⁴, F. Lucarelli⁵⁶, W. Luszczak^{16,17}, Y. Lyu^{15,49}, J. Madsen⁴, K. B. M. Mahn⁴¹, Y. Makino⁴, E. Manao²⁰, S. Mancina^{4,24}, W. Marie Sainte⁴, I. C. Mariş⁵, S. Marka⁵⁷, Z. Marka⁵⁷, M. Marsee³⁸, I. Martinez-Soler¹¹, R. Maruyama⁵⁸, F. Mayhew⁴¹, T. McElroy⁵³, F. McNally⁵⁹, J. V. Mead⁶, K. Meagher⁴, S. Mechbal², A. Medina¹⁷, M. Meier⁴⁴, Y. Mercck³⁵, L. Merten¹⁸, J. Micallef⁴¹, J. Mitchell⁴⁵, T. Montaruli⁵⁶, R. W. Moore⁵³, Y. Morii⁴⁴, R. Morse⁴, M. Moulai⁴, T. Mukherjee²⁶, R. Naab², R. Nagai⁴⁴, M. Nakos⁴, U. Naumann⁴², J. Necker², A. Negi⁵², M. Neumann³⁰, H. Niederhausen⁴¹, M. U. Nisa⁴¹, A. Noell²¹, A. Novikov⁸, S. C. Nowicki⁴¹, A. Obertacke Pollmann⁴⁴, V. O'Dell⁴, M. Oehler²⁶, B. Oeyen⁶⁰, A. Olivas²³, R. Orsoe²⁰, J. Osborn⁴, E. O'Sullivan¹⁹, H. Pandya⁸, N. Park⁵⁰, G. K. Parker⁵², E. N. Paudel⁸, L. Paul¹³, C. Pérez de los Heros¹⁹, J. Peterson⁴, S. Philippen²¹, A. Pizzuto⁴, M. Plum¹³, A. Pontén¹⁹, Y. Popovych²⁷, M. Prado Rodriguez⁴, B. Pries⁴¹, R. Procter-Murphy²³, G. T. Przybylski⁴⁹, C. Raab⁴⁰, J. Rack-Helleis²⁷, K. Rawlins⁶¹, Z. Rechav⁴, A. Rehman⁸, P. Reichherzer¹⁸, G. Renzi⁵, E. Resconi²⁰, S. Reusch², W. Rhode⁷, B. Riedel⁴, A. Rifaie²¹, E. J. Roberts²⁹, S. Robertson^{15,49}, S. Rodan³³, G. Roellinghoff³³, M. Rongen¹⁰, C. Rott^{12,33}, T. Ruhe⁷, L. Ruohan²⁰, D. Ryckbosch⁶⁰, I. Safa^{4,11}, J. Saffer⁴³, D. Salazar-Gallegos⁴¹, P. Sampathkumar²⁶, S. E. Sanchez Herrera⁴¹, A. Sandrock⁴², M. Santander³⁸, S. Sarkar⁵³, S. Sarkar⁶², J. Savelberg²¹, P. Savina⁴, M. Schaufel²¹, H. Schieler²⁶, S. Schindler¹⁰, L. Schlickmann²¹, B. Schlüter³⁰, F. Schlüter⁵, N. Schmeisser⁴², T. Schmidt²³, J. Schneider¹⁰, F. G. Schröder^{8,26}, L. Schumacher¹⁰, G. Schwefer²¹, S. Sclafani²³, D. Seckel⁸, M. Seikh²⁵, S. Seunarine⁶³, R. Shah³¹, S. Shefali⁴³, N. Shimizu⁴⁴, M. Silva⁴, B. Skrzypek¹¹, B. Smithers⁵², R. Snihur⁴, J. Soedingrekso⁷, A. Søgaard⁶, D. Soldin⁴³, P. Soldin²¹, G. Sommani¹⁸, C. Spannfellner²⁰, G. M. Spiczak⁶³, C. Spiering², M. Stamatikos¹⁷, T. Stanev⁸, T. Stezelberger⁴⁹, T. Stürwald⁴², T. Stuttard⁶, G. W. Sullivan²³, I. Taboada²⁸, S. Ter-Antonyan⁴⁵, M. Thiesmeyer²¹, W. G. Thompson¹¹, J. Thwaites⁴, S. Tilav⁸, K. Tollefson⁴¹, C. Tönnis³³, S. Toscano⁵, D. Tosi⁴, A. Trettin², C. F. Tung²⁸, R. Turcotte²⁶, J. P. Twagirayezu⁴¹, M. A. Unland Elorrieta³⁰, A. K. Upadhyay^{4,64}, K. Upshaw⁴⁵, A. Vaidyanathan⁹, N. Valtonen-Mattila¹⁹, J. Vandenbroucke⁴, N. van Eijndhoven³⁵, D. Vannerom³⁴, J. van Santen², J. Vara³⁰, J. Veitch-Michaelis⁴, M. Venugopal²⁶, M. Vereecken⁴⁰, S. Verpoest⁸, D. Veske⁵⁷, A. Vijai²³, C. Walck³⁹, C. Weaver⁴¹, P. Weigel³⁴, A. Weindl²⁶, J. Weldert³⁷, A. Y. Wen¹¹, C. Wendt⁴, J. Werthebach⁷, M. Weyrauch²⁶, N. Whitehorn⁴¹, C. H. Wiebusch²¹, D. R. Williams³⁸

L. Witthaus⁷, A. Wolf²¹, M. Wolf²⁰ , G. Wrede¹⁰, X. W. Xu⁴⁵, J. P. Yanez⁵³, E. Yildizci⁴, S. Yoshida⁴⁴ , R. Young²⁵, S. Yu⁴¹,
T. Yuan⁴ , Z. Zhang³² , P. Zhelnin¹¹, P. Zilberman⁴, and M. Zimmerman⁴

IceCube Collaboration

- ¹ Department of Physics, Loyola University Chicago, Chicago, IL 60660, USA; analysis@icecube.wisc.edu
² Deutsches Elektronen-Synchrotron DESY, Platanenallee 6, D-15738 Zeuthen, Germany
³ Department of Physics and Astronomy, University of Canterbury, Private Bag 4800, Christchurch, New Zealand
⁴ Department of Physics and Wisconsin IceCube Particle Astrophysics Center, University of Wisconsin–Madison, Madison, WI 53706, USA
⁵ Université Libre de Bruxelles, Science Faculty CP230, B-1050 Brussels, Belgium
⁶ Niels Bohr Institute, University of Copenhagen, DK-2100 Copenhagen, Denmark
⁷ Department of Physics, TU Dortmund University, D-44221 Dortmund, Germany
⁸ Bartol Research Institute and Department of Physics and Astronomy, University of Delaware, Newark, DE 19716, USA
⁹ Department of Physics, Marquette University, Milwaukee, WI 53201, USA
¹⁰ Erlangen Centre for Astroparticle Physics, Friedrich-Alexander-Universität Erlangen-Nürnberg, D-91058 Erlangen, Germany
¹¹ Department of Physics and Laboratory for Particle Physics and Cosmology, Harvard University, Cambridge, MA 02138, USA
¹² Department of Physics and Astronomy, University of Utah, Salt Lake City, UT 84112, USA
¹³ Physics Department, South Dakota School of Mines and Technology, Rapid City, SD 57701, USA
¹⁴ Department of Physics and Astronomy, University of California, Irvine, CA 92697, USA
¹⁵ Department of Physics, University of California, Berkeley, CA 94720, USA
¹⁶ Department of Astronomy, Ohio State University, Columbus, OH 43210, USA
¹⁷ Department of Physics and Center for Cosmology and Astro-Particle Physics, Ohio State University, Columbus, OH 43210, USA
¹⁸ Fakultät für Physik & Astronomie, Ruhr-Universität Bochum, D-44780 Bochum, Germany
¹⁹ Department of Physics and Astronomy, Uppsala University, Box 516, SE-75120 Uppsala, Sweden
²⁰ Physik-department, Technische Universität München, D-85748 Garching, Germany
²¹ III. Physikalisches Institut, RWTH Aachen University, D-52056 Aachen, Germany
²² Department of Physics and Astronomy, University of Rochester, Rochester, NY 14627, USA
²³ Department of Physics, University of Maryland, College Park, MD 20742, USA
²⁴ Dipartimento di Fisica e Astronomia Galileo Galilei, Università Degli Studi di Padova, I-35122 Padova PD, Italy
²⁵ Department of Physics and Astronomy, University of Kansas, Lawrence, KS 66045, USA
²⁶ Karlsruhe Institute of Technology, Institute for Astroparticle Physics, D-76021 Karlsruhe, Germany
²⁷ Institute of Physics, University of Mainz, Staudinger Weg 7, D-55099 Mainz, Germany
²⁸ School of Physics and Center for Relativistic Astrophysics, Georgia Institute of Technology, Atlanta, GA 30332, USA
²⁹ Department of Physics, University of Adelaide, Adelaide, 5005, Australia
³⁰ Institut für Kernphysik, Westfälische Wilhelms-Universität Münster, D-48149 Münster, Germany
³¹ Department of Physics, Drexel University, 3141 Chestnut Street, Philadelphia, PA 19104, USA
³² Department of Physics and Astronomy, Stony Brook University, Stony Brook, NY 11794-3800, USA
³³ Department of Physics, Sungkyunkwan University, Suwon 16419, Republic of Korea
³⁴ Department of Physics, Massachusetts Institute of Technology, Cambridge, MA 02139, USA
³⁵ Vrije Universiteit Brussel (VUB), Dienst ELEM, B-1050 Brussels, Belgium
³⁶ Department of Astronomy and Astrophysics, Pennsylvania State University, University Park, PA 16802, USA
³⁷ Department of Physics, Pennsylvania State University, University Park, PA 16802, USA
³⁸ Department of Physics and Astronomy, University of Alabama, Tuscaloosa, AL 35487, USA
³⁹ Oskar Klein Centre and Department of Physics, Stockholm University, SE-10691 Stockholm, Sweden
⁴⁰ Centre for Cosmology, Particle Physics and Phenomenology—CP3, Université catholique de Louvain, Louvain-la-Neuve, Belgium
⁴¹ Department of Physics and Astronomy, Michigan State University, East Lansing, MI 48824, USA
⁴² Department of Physics, University of Wuppertal, D-42119 Wuppertal, Germany
⁴³ Karlsruhe Institute of Technology, Institute of Experimental Particle Physics, D-76021 Karlsruhe, Germany
⁴⁴ Department of Physics and The International Center for Hadron Astrophysics, Chiba University, Chiba 263-8522, Japan
⁴⁵ Department of Physics, Southern University, Baton Rouge, LA 70813, USA
⁴⁶ Institute of Physics, Academia Sinica, Taipei, 11529, Taiwan
⁴⁷ Institut für Physik, Humboldt-Universität zu Berlin, D-12489 Berlin, Germany
⁴⁸ Department of Astronomy, University of Wisconsin–Madison, Madison, WI 53706, USA
⁴⁹ Lawrence Berkeley National Laboratory, Berkeley, CA 94720, USA
⁵⁰ Department of Physics, Engineering Physics, and Astronomy, Queen’s University, Kingston, ON K7L 3N6, Canada
⁵¹ CTSPS, Clark-Atlanta University, Atlanta, GA 30314, USA
⁵² Department of Physics, University of Texas at Arlington, 502 Yates Street, Science Hall Room 108, Box 19059, Arlington, TX 76019, USA
⁵³ Department of Physics, University of Alberta, Edmonton, AB T6G 2E1, Canada
⁵⁴ Department of Physics & Astronomy, University of Nevada, Las Vegas, NV 89154, USA
⁵⁵ Nevada Center for Astrophysics, University of Nevada, Las Vegas, NV 89154, USA
⁵⁶ Département de physique nucléaire et corpusculaire, Université de Genève, CH-1211 Genève, Switzerland
⁵⁷ Columbia Astrophysics and Nevis Laboratories, Columbia University, New York, NY 10027, USA
⁵⁸ Department of Physics, Yale University, New Haven, CT 06520, USA
⁵⁹ Department of Physics, Mercer University, Macon, GA 31207-0001, USA
⁶⁰ Department of Physics and Astronomy, University of Gent, B-9000 Gent, Belgium
⁶¹ Department of Physics and Astronomy, University of Alaska Anchorage, 3211 Providence Drive, Anchorage, AK 99508, USA

⁶²Department of Physics, University of Oxford, Parks Road, Oxford OX1 3PU, UK⁶³Department of Physics, University of Wisconsin, River Falls, WI 54022, USA

Received 2023 September 21; revised 2023 December 13; accepted 2023 December 14; published 2024 March 13

Abstract

IceCube alert events are neutrinos with a moderate-to-high probability of having astrophysical origin. In this study, we analyze 11 yr of IceCube data and investigate 122 alert events and a selection of high-energy tracks detected between 2009 and the end of 2021. This high-energy event selection (alert events + high-energy tracks) has an average probability of ≥ 0.5 of being of astrophysical origin. We search for additional continuous and transient neutrino emission within the high-energy events' error regions. We find no evidence for significant continuous neutrino emission from any of the alert event directions. The only locally significant neutrino emission is the transient emission associated with the blazar TXS 0506+056, with a local significance of 3σ , which confirms previous IceCube studies. When correcting for 122 test positions, the global p -value is 0.156 and compatible with the background hypothesis. We constrain the total continuous flux emitted from all 122 test positions at 100 TeV to be below $1.2 \times 10^{-15} (\text{TeV cm}^2 \text{s})^{-1}$ at 90% confidence assuming an E^{-2} spectrum. This corresponds to 4.5% of IceCube's astrophysical diffuse flux. Overall, we find no indication that alert events in general are linked to lower-energy continuous or transient neutrino emission.

Unified Astronomy Thesaurus concepts: High energy astrophysics (739); Active galactic nuclei (16); Neutrino astronomy (1100); Transient sources (1851); Blazars (164)

1. Introduction

The IceCube Neutrino Observatory (Aartsen et al. 2017a) is a Cherenkov detector using a cubic kilometer of Antarctic ice at the geographic South Pole to primarily (but not exclusively) study high-energy astrophysical neutrinos. Its duty cycle is greater than 99% (Aartsen et al. 2017a), and its field of view covers the full sky while being most sensitive to high-energy neutrino events near the celestial equator. This makes IceCube ideal for surveying the sky (Aartsen et al. 2017b). As part of the real-time program, IceCube alerts other telescopes upon detection of a neutrino event with a high probability of being of astrophysical origin, which can then trigger follow-up observations (Kintscher 2016; Aartsen et al. 2017b; Blaufuss et al. 2019).

On 2017 September 22, IceCube detected a neutrino of likely astrophysical origin (IceCube-170922A⁶⁷). This triggered multiwavelength follow-up observations, which detected a flaring blazar (TXS 0506+056) at the reconstructed origin direction of IceCube-170922A (Aartsen et al. 2018a). This correlation is significant at a 3σ level (Aartsen et al. 2018a). Additionally, a neutrino flare was identified originating from the same direction between 2014 September and 2015 March with a significance of 3.5σ (Aartsen et al. 2018b).

This detection demonstrates that IceCube alerts can point to neutrino source candidates due to their high probability of being of astrophysical origin, and we aim to investigate the origin directions of other IceCube alerts. A preliminary search showed no indication of continuous neutrino emission (Karl 2019). However, the IceCube alert criteria have since been updated (Blaufuss et al. 2019; Abbasi et al. 2023a). The

IceCube data have also been reprocessed with improved calibration of the optical sensors (Aartsen et al. 2020; Abbasi et al. 2021a). This leads to improved energy and direction reconstruction compared to previous results in Aartsen et al. (2015, 2018b, 2020) and Abbasi et al. (2021b, 2021c, 2021d). A first analysis benefiting from this new processing (Abbasi et al. 2022a) detected the neutrino signal from the Seyfert II galaxy NGC 1068 with a significance of 4.2σ (compared to 2.9σ in Aartsen et al. 2020). A large part of the increase (0.9σ) is due to improved data processing and calibration. More details about effects on the data are discussed in Appendix B and the supplementary material of Abbasi et al. (2022a).

In this work, we analyze 11 yr of reprocessed IceCube data (throughgoing muon tracks; see Table 1) and search for an excess of neutrino-induced muons. We apply a conservative lower limit on the angular uncertainty of $0^\circ.2$, whereas the median angular resolution is $0^\circ.57$ (compared to a median angular resolution of $0^\circ.59$ before the reprocessing). We identify possible neutrino production sites by looking at the origin of high-energy neutrinos that have a high probability of being of astrophysical origin. IceCube's highest-energy neutrinos with the largest astrophysical purity are events from the new selection of IceCube alerts published in the so-called "gold" alert channel (Blaufuss et al. 2019; Abbasi et al. 2023a). Additionally, we extend the list by including 18 high-energy events from Abbasi et al. (2022b) that were confirmed to be likely astrophysical events by a new event classifier (Kronmueller & Glauch 2019). Since we use a combination of IceCube alert events and high-energy tracks identified retrospectively, we will refer to our event selection as "alert+ events" for brevity. All IceCube data used in this work (lower- and high-energy events) have been reprocessed.

In this work, we excluded alert+ events within 30° of the geographic poles (affecting three events), for which we have smaller statistics for the background. Other IceCube analyses have applied different decl. cuts (for example, including all events up to 81° decl., Abbasi et al. 2022a, or up to 82° , Aartsen et al. 2020). Additionally, we removed alert+ events with large uncertainties ($\geq 100c \text{ deg}^2$, affecting two events). As a result, our final sample consists of 122 high-energy events (104 IceCube alert events and 18 high-energy tracks, listed in Table 3), detected between 2009 and the end of 2021. On

⁶⁴ Also at Institute of Physics, Sachivalaya Marg, Sainik School Post, Bhubaneswar 751005, India.

⁶⁵ Also at Department of Space, Earth and Environment, Chalmers University of Technology, 412 96 Gothenburg, Sweden.

⁶⁶ Also at Earthquake Research Institute, University of Tokyo, Bunkyo, Tokyo 113-0032, Japan.

⁶⁷ https://gc.gsfc.nasa.gov/notices_amon/50579430_130033.amon



Table 1
Overview of the Improved and Reprocessed Data Samples in This Analysis

| Year | Livetime (days) | Number of Events | Start | End |
|-----------------|--------------------|------------------|-------------|-------------|
| IC 59 | 353.578 | 107,011 | 2009 May 5 | 2010 May 31 |
| IC 79 | 316.045 | 93,133 | 2010 Jun 1 | 2011 May 13 |
| IC 86 2011–2019 | 3184.163 | 1,133,364 | 2011 May 13 | 2020 May 29 |

Note. The columns list the configuration of the detector (“IC” and the number of deployed strings), the uptime (livetime) of the detector in days, the number of events in each sample, and the start and end dates of the data subset.

average, our selected alert+ events have a probability of being astrophysical of $\gtrsim 0.5$. The probability of being astrophysical is spectrum-dependent and based on the muon neutrino spectrum measured by IceCube (Haack & Wiebusch 2017; Abbasi et al. 2022b). The median angular resolution (90% uncertainty regions) of alert+ events is $2^\circ.1$. In Figure 1, we show a map of all arrival directions and their 90% uncertainty regions of IceCube alert+ events investigated in this work. These events provide positions of interest analogous to a catalog of possible neutrino sources. Since IceCube alert+ events trigger this analysis, we remove the respective alert+ event from the 11 yr of IceCube data when running the analysis. We present the analysis method in Section 2 and the results in Section 3.

2. Analysis Method

We use an unbinned likelihood approach as presented by Braun et al. (2008). In this work, we investigate two source types: continuous sources and transient sources. We compare two hypotheses (each with a set of parameters θ).

1. *Background hypothesis* $H_0(\theta_0)$. The background comprises atmospheric neutrinos, atmospheric muons (remaining after event selection cuts), and diffuse astrophysical neutrinos. The flux is uniform in time and R.A.
2. *Signal hypothesis* $H_1(\theta_1)$. There is a signal component in addition to the atmospheric background and the average diffuse astrophysical neutrino emission. The signal neutrinos cluster around their source (subscript S) at R. A., decl. $\mathbf{x}_S = (\alpha_S, \delta_S)$. The energy spectrum of the emitted flux is an unbroken power law: $\frac{d\phi}{dE_\nu} \propto E_\nu^{-\gamma}$. In the specific case of a transient source hypothesis (see Section 2.2), the neutrino emission has a Gaussian time profile with mean μ_T and width σ_T .

We remove the high-energy alert+ events that triggered this analysis from the data set. Hence, we look for additional neutrino emission from the direction of the high-energy alert+ events. We then maximize the likelihood, \mathcal{L} , and compute the likelihood ratio,

$$\lambda(\mathbf{x}) = \frac{\sup \mathcal{L}(H_0)}{\sup \mathcal{L}(H_1)}. \quad (1)$$

The likelihood maximization varies the expectation value of the number of detected signal neutrinos, n_S , and the emitted energy spectral index, γ . We allow values for γ between 1.5 and 4. For the background hypothesis, n_S is fixed to 0.

The likelihood is the probability density of observing the data given a specific hypothesis. The probability density of observing an event, i , is a sum of its probability to be signal, S_i ,

or background, B_i : $\frac{n_S}{N}S_i + \left(1 - \frac{n_S}{N}\right)B_i$, where N is the total number of detected events (signal and background combined).

We define the test statistic (TS) as

$$\begin{aligned} \text{TS} &= -2 \ln \lambda = -2 \ln \left[\frac{\mathcal{L}(\hat{\theta}_0 | \mathbf{x}_S)}{\mathcal{L}(\hat{\theta}_1 | \mathbf{x}_S)} \right] = 2 \ln \left[\frac{\mathcal{L}(n_S = \hat{n}_S)}{\mathcal{L}(n_S = 0)} \right] \\ &= 2 \sum_i \ln \left[\frac{\hat{n}_S}{N} \left(\frac{S_i}{B_i} - 1 \right) + 1 \right] \end{aligned} \quad (2)$$

for a signal hypothesis with the best-fit value of \hat{n}_S neutrinos (where the “ $\hat{\cdot}$ ” denotes the best fit of a parameter) as the mean number of neutrinos we expect to detect from the neutrino source.

The investigated source candidates have directional uncertainties (see Figure 1). However, we assume that potential sources are smaller than the best resolution of $0^\circ.2$ in our data (TXS 0506+056 has an angular size of $\sim 2''.6$). Hence, we fit the best point-source position within a reconstructed 90% uncertainty region by dividing the region into a grid with steps of $0^\circ.2$ in R.A. and decl., the best angular uncertainty for events used in this study. The likelihood is optimized at each grid point. The grid point yielding the best result (i.e., the highest TS value) is subsequently considered the point-source position.

This procedure is run on different realizations of background data $\sim 10^4$ times. The background data are all 11 yr of muon tracks with randomly assigned right ascensions. In the final step, we calculate the TS value, TS_{data} , for the true data and compare this with the simulated background TS distribution. The local p -value is the probability of getting this TS_{data} (or a larger value) from a random background realization. This procedure is repeated for all remaining regions in the sky, yielding 122 local p -values. From these 122 values, we take the most significant local p -value, p_0 , to identify the most significant source.

As a next step, we correct the significance for having tested 122 regions in the sky. Considering only background realizations, we take the most significant p -value out of 122 positions for each realization and generate a distribution of best local p -values, $p_{0,\text{BG}}$. The final global p -value of our analysis is the probability of $p_{0,\text{BG}}$ being at least as significant as the p -value we got from our real data, p_0 . Since we are investigating only a limited number of points (122), weaker neutrino emissions have a higher significance in this analysis than in an all-sky scan, for example, in Abbasi et al. (2022a).

When testing the method with Monte Carlo simulations, the best-fit number of signal neutrinos, \hat{n}_S , and source spectral index, $\hat{\gamma}$, show a bias compared to the true simulated source properties. For sources with simulated hard spectral indices (i.e., $\gamma = 2$), there is a tendency to fit slightly softer spectra and

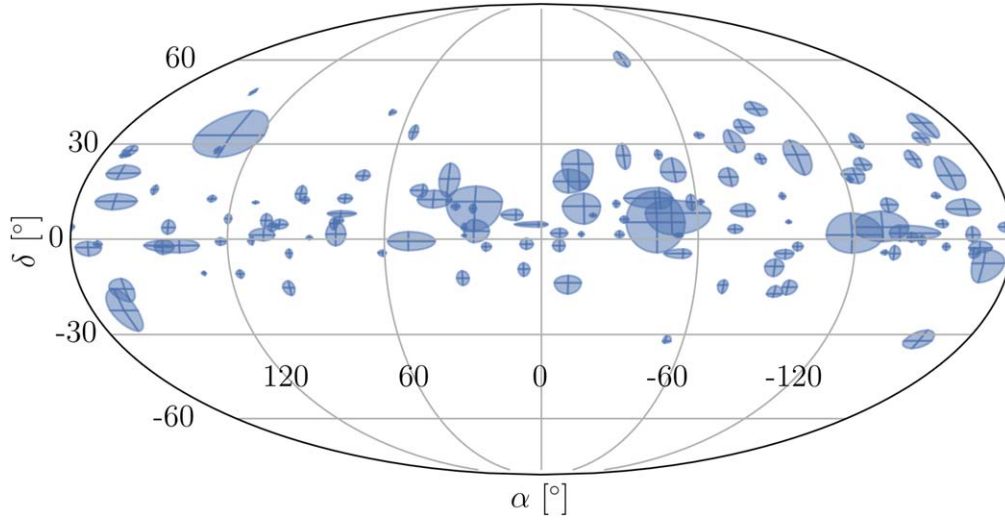


Figure 1. Sky map in R.A. and decl. (epoch = J2000) with the arrival directions of events fulfilling the IceCube alert criteria (with the highest probability of being of astrophysical origin) we investigate in this work. The events were detected between 2009 August and the end of 2021. The shaded regions represent the 90% uncertainty region of the reconstruction.

a slightly larger number of signal neutrinos. For simulated sources following softer spectral indices (i.e., $\gamma = 3$), the tendency is reversed to fitting slightly harder spectral indices and smaller numbers of signal neutrinos. Appendix A presents a more in-depth discussion of this bias. Correcting the bias is not straightforward, and we have decided not to include an at best incomplete correction. Hence, the best-fit fluxes are only indicative. This bias does not affect the flux limits since they are based on simulated fluxes where the true source strength is known.

2.1. Time-integrated Search for Continuous Sources

We define the signal and background probability density functions (pdfs) S_i and B_i in spatial and energy parts (see, e.g., Braun et al. 2008; Abbasi et al. 2011). The spatial part depends on the source position \mathbf{x}_S and the reconstructed event properties: the reconstructed origin \mathbf{x}_i and the angular uncertainty of the reconstructed origin σ_i . The energy part depends on the reconstructed muon energy, E_i ; the reconstructed origin decl., δ_i ; and the source energy spectral index, γ . The signal pdf for a steady source is hence

$$\begin{aligned} S_i(\mathbf{x}_i, E_i | \sigma_i, \mathbf{x}_S, \gamma) &= S_{\text{spatial}}(\mathbf{x}_i | \sigma_i, \mathbf{x}_S) \cdot S_{\text{energy}}(E_i | \delta_i, \gamma) \\ &= \frac{1}{2\pi\sigma_i^2} \exp\left(-\frac{|\mathbf{x}_i - \mathbf{x}_S|^2}{2\sigma_i^2}\right) \cdot S_{\text{energy}}(E_i | \delta_i, \gamma). \end{aligned} \quad (3)$$

The energy pdf, S_{energy} , is the probability of detecting a neutrino with reconstructed energy, E_i , at decl., δ_i , assuming the source emits neutrinos with a spectrum of $E^{-\gamma}$. The background pdfs, B_i , are defined similarly:

$$\begin{aligned} B_i(\mathbf{x}_i, E_i) &= B_{\text{spatial}}(\mathbf{x}_i) \cdot B_{\text{energy}}(E_i | \delta_i) \\ &= \frac{1}{2\pi} \cdot P(\delta_i) \cdot B_{\text{energy}}(E_i | \delta_i). \end{aligned} \quad (4)$$

The spatial term depends only on the event decl., δ_i . We assume uniformity in R.A. for the background data due to IceCube's unique position at the South Pole. B_{energy} is derived directly from experimental data.

Searching for neutrino counterparts of the alert+ events, we want to be sensitive to a single strong emission from one source (or a few sources) and, additionally, to faint emissions from a larger number of sources. Hence, our search for continuous sources consists of two parts. The first part searches for single strong neutrino emitters. The second part investigates the overall neutrino emission from all 122 positions of interest. In the latter case, we combine the neutrino emission and define a new TS value, $\text{TS}_{\text{stacked}}$, by summing the TS values of all alert+ positions, k ,

$$\text{TS}_{\text{stacked}} = \sum_k \text{TS}_k. \quad (5)$$

We take the TS_k from the individual search; hence, we do not correct for overlapping uncertainty regions of alert+ events.

2.2. Transient Sources

For transient sources, we multiply a temporal pdf with the previously defined spatial and energy pdfs in Equations (3) and (4) (Braun et al. 2010). We assume a Gaussian-shaped time profile centered around μ_T with width σ_T for the signal part. The temporal signal pdf becomes

$$S_T(t_i | \mu_T, \sigma_T) = \frac{1}{\sigma_T \sqrt{2\pi}} \exp\left(-\frac{(t_i - \mu_T)^2}{2\sigma_T^2}\right), \quad (6)$$

with t_i as the time the event was detected. The background expectation is a constant rate over the whole data-taking time, t_{data} :

$$B_T = \frac{1}{t_{\text{data}}}. \quad (7)$$

The search for time-dependent sources adds another optimization step for the best flaring time. This introduces a bias toward shorter flares since the number of possible shorter flares is larger than the number of possible longer flares. We correct for this effect by multiplying the TS by a marginalization factor, $\frac{\sqrt{2\pi}\sigma_T}{300 \text{ days}}$ (Braun et al. 2010). Here, 300 days is the maximal flaring time. Longer timescales would result in

worse sensitivity than the time-integrated search. We assume a minimal σ_T of 5 days to ensure the background uniformity in R.A.

Conventional methods to find neutrino flares as in Aartsen et al. (2015, 2018b) and Abbasi et al. (2021c, 2021d) apply a brute-force scan of all possible time intervals between events where the ratio of Equation (3) over Equation (4) exceeds a certain threshold. This is computationally expensive. The computational cost can be reduced by increasing the required threshold and hence reducing the possible number of intervals scanned. We want to include as few biases as possible, and if following conventional approaches, we would apply the same threshold as in Aartsen et al. (2018b), where the ratio had to be ≥ 1 . However, Aartsen et al. (2018b) performs this search only on one position in the sky. In our case, this would mean scanning the uncertainty region of 122 alert+ events in steps of 0.2° and, at each step, evaluating every possible time window between 5 and 300 days in 11 yr for neutrino emission. This proved to be computationally unfeasible. To overcome this problem, we investigated new approaches (Karl et al. 2021, 2023; Karl 2022) that do not rely on thresholds, such as a different TS to evaluate if an emission is time-dependent (Eller & Shtembari 2023) or finding an analytical description of the TS such that we would not need to simulate a large number of background and signal models.

Here, we have applied an unsupervised-learning algorithm looking for clustering in data: expectation maximization (Dempster et al. 1977). This is the first time we apply expectation maximization to IceCube data and use it to fit the best time of transient neutrino emission.

The procedure is as follows (Karl & Eller 2023). For a source position to be tested (grid point), we assume a two-component mixture model for the temporal distribution of our data (a neutrino flare in the form of a Gaussian signal and uniform background). As a starting flare, we choose a single very broad flare, extending beyond the whole data-taking period. For each event, we compute the probability of it belonging to the neutrino flare (the membership probability). These probabilities are then used to improve the flare parameters iteratively. In the calculation of the membership probability for event i , we include the pdf values for the spatial and energy signal and background pdfs (as in Equations (3) and (4)) as event weights. The membership probability is

$$\begin{aligned} P_{i,\text{flare}} &= \frac{\frac{n_{\text{flare}}}{N} S_i S_T(t_i | \mu_T, \sigma_T)}{\frac{n_{\text{flare}}}{N} S_i S_T(t_i | \mu_T, \sigma_T) + (1 - \frac{n_{\text{flare}}}{N}) B_i B_T} \\ &= \frac{n_{\text{flare}} \frac{S_i}{B_i} S_T(t_i | \mu_T, \sigma_T)}{n_{\text{flare}} \frac{S_i}{B_i} S_T(t_i | \mu_T, \sigma_T) + \frac{N - n_{\text{flare}}}{t_{\text{data}}}}, \end{aligned} \quad (8)$$

and at each iteration, the mean time, μ_T , and the width, σ_T , are recalculated using

$$\mu_T = \frac{\sum_i P_{i,\text{flare}} t_i}{\sum_i P_{i,\text{flare}}} \quad (9)$$

and

$$\sigma_T = \frac{\sum_i P_{i,\text{flare}} (t_i - \mu_T)^2}{\sum_i P_{i,\text{flare}}}. \quad (10)$$

The quantity n_{flare} scales the Gaussian temporal pdf according to the expected number of signal events. However, n_{flare} is only

used to determine μ_T and σ_T ; n_S is fitted independently once we determine the time pdf of the neutrino flare. We stop the iterations when there is no change in the likelihood in the past 20 iterations or once 500 iterations have been performed.

The signal weight, S_i/B_i , depends on the assumed source spectral index, γ . We want to avoid favoring a specific index; hence, we run expectation maximization for different fixed spectral indices, γ_{EM} , between 1.5 and 4 in steps of 0.2 (Karl & Eller 2023). We get an optimized time pdf for each γ_{EM} . We then optimize the TS as in Equation (2) with the signal and background pdfs, including the temporal pdfs for each γ_{EM} . In this step, we fit n_S and γ while keeping the temporal pdf with $\hat{\mu}_T(\gamma_{\text{EM}})$ and $\hat{\sigma}_T(\gamma_{\text{EM}})$ fixed. The flare yielding the highest TS value is then the best-fit flare for this grid point. For each alert +, we repeat this procedure at every grid point in the uncertainty region. The point with the most significant result is then the preferred source location. For the background TS distribution, we shuffled the event times and calculated the new R.A. values based on the event azimuths and the shuffled times.

3. Results

3.1. Continuous Sources

The search for the strongest single continuous source yields a global p -value of 0.98 and is compatible with the background hypothesis. We determine an upper flux limit by simulating neutrino emission with an E^{-2} spectrum. The upper flux limit is the flux for which 90% of the corresponding TS distribution lies above the TS value of the strongest single continuous source. We get an upper flux limit (for muon neutrinos and antineutrinos) at a 90% confidence level for the most significant position of $\Phi_{90\%,100\text{ TeV}}^{\nu_\mu + \bar{\nu}_\mu, \text{single}} = 6.9 \times 10^{-17} (\text{TeV cm}^2 \text{s})^{-1}$. In general, the energy-dependent flux, $\Phi(E)$, of this flux limit is $\Phi(E) = \Phi_{90\%,100\text{ TeV}}^{\nu_\mu + \bar{\nu}_\mu, \text{single}} \times \left(\frac{E}{100\text{ TeV}}\right)^{-2}$. The acceptance for the simulated flux has a limited range in energy. We define the energy range for the flux limit as the central 90% quantile of detected simulated events. In this case, we limit the flux from 0.9 to 483 TeV. Table 4 lists the results for all 122 investigated regions.

For the combined emission of all sources, we get a p -value of 8%, which is also compatible with the background hypothesis. We determine the 90% confidence level upper flux limit, $\Phi_{90\%,100\text{ TeV}}^{\nu_\mu + \bar{\nu}_\mu, \text{stacked}}$, by simulating an increasing number of sources emitting a weak flux, ϕ_1 , corresponding to one neutrino coming from a source at the celestial equator—IceCube’s most sensitive region for detecting neutrinos at the highest energies—in 11 yr ($\phi_1 = 4.502 \times 10^{-18} (\text{TeV cm}^2 \text{s})^{-1}$). We repeat the simulation $\sim 10^4$ times for each combined flux and create a $\text{TS}_{\text{stacked}}$ distribution. Based on this distribution, we determine the combined flux that is strong enough to yield a higher TS value than our result with 90% probability.

The upper limit of emission additional to the alert+ events is $\Phi_{90\%,100\text{ TeV}}^{\nu_\mu + \bar{\nu}_\mu, \text{stacked}} = 4.2 \times 10^{-16} (\text{TeV cm}^2 \text{s})^{-1}$ for a spectral index of $\gamma = 2$ and within the energy range from 4.2 TeV to 3.6 PeV. For comparison, the diffuse astrophysical neutrino flux is $\Phi_{\text{diffuse},100\text{ TeV}} = 1.44 \times 10^{-15} (\text{TeV cm}^2 \text{s sr})^{-1}$ in the range of 15 TeV to 5 PeV (Abbasi et al. 2022b) with a spectral index of $\gamma = 2.37$. Integrating over the energy range where both the diffuse flux and $\Phi_{90\%,100\text{ TeV}}^{\nu_\mu + \bar{\nu}_\mu, \text{stacked}}$ overlap, $\Phi_{90\%,100\text{ TeV}}^{\nu_\mu + \bar{\nu}_\mu, \text{stacked}}$ corresponds to 1.6% of the astrophysical diffuse flux. To constrain the maximal possible emission from the alert+ regions, including

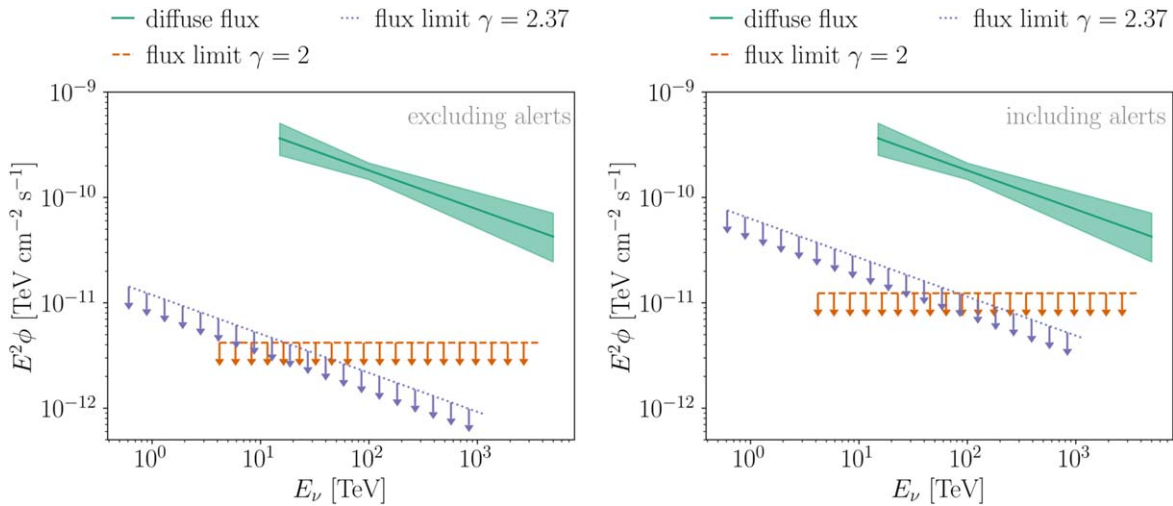


Figure 2. 90% confidence level upper flux limits for all source candidates combined (dashed orange line) valid in the energy range of 4.2 TeV to 3.6 PeV and a neutrino emission following E^{-2} . The green line is the diffuse astrophysical neutrino flux ($\Phi_{\text{diffuse}, 100 \text{ TeV}} = 1.44 \times 10^{-15} \cdot 4\pi (\text{TeV cm}^2 \text{s})^{-1}$) in the range of 15 TeV to 5 PeV (Abbasi et al. 2022b). The dotted purple line shows the 90% confidence level upper flux limit combining all sources for the spectral index of the diffuse flux ($\gamma = 2.37$) between 0.6 TeV and 1 PeV. Left: the upper flux limit, excluding the alert+ events in the analyzed data, is 1.6% ($\gamma = 2$) of the astrophysical diffuse flux in the overlapping energy range and 1.5% when assuming the same spectral index ($\gamma = 2.37$) as for the astrophysical diffuse flux. Right: the upper flux limit, including the alert+ events in the data, is 4.5% of the astrophysical diffuse flux in the overlapping energy range for $\gamma = 2$ and 8% of the diffuse flux when assuming the same spectral index ($\gamma = 2.37$) as for the astrophysical diffuse flux.

the highest-energy events, we include the alert+ events just for the following limit. Thus, considering the total emission of all 122 regions, including alert+ events, we get an upper flux limit of $\Phi_{90\%, 100 \text{ TeV}}^{\nu_{\mu} + \nu_{\tau}, \text{with alerts}} = 1.2 \times 10^{-15} (\text{TeV cm}^2 \text{s})^{-1}$ for the energy range from 4.2 TeV to 3.6 PeV, which corresponds to 4.5% of the diffuse astrophysical neutrino flux where both fluxes overlap in their energy range (see Figure 2). We repeat the upper flux limit calculation with the same spectral index as for the astrophysical diffuse flux and get a limit of $2.1 \times 10^{-16} (\text{TeV cm}^2 \text{s})^{-1}$ (1.5% of the astrophysical diffuse flux) excluding alert+ events and $1.1 \times 10^{-15} (\text{TeV cm}^2 \text{s})^{-1}$ including alert+ events (8% of the astrophysical diffuse flux) at 100 TeV. For $\gamma = 2.37$, the energies of the simulated detected events range from 0.6 TeV to 1 PeV. This energy range differs from the previous range for $\gamma = 2$. The energy distribution of the signal events depends on the simulated energy spectral index. There are more neutrinos in lower energies if the simulated energy spectrum is softer compared to a harder emission.

The lack of lower-energy neutrino emission (compared to IceCube alert+ events) could be caused by various scenarios. It is, for example, possible that some sources flare in neutrinos, emitting mainly high-energy neutrinos. Another possibility might be a hard neutrino emission, i.e., $\gamma \leq 1$ (for example, models proposed in Waxman & Bahcall 1999; Padovani et al. 2022). The atmospheric background would dominate the lower-energy neutrino emission. The higher-energy neutrino emission would be detected as single high-energy events, given IceCube’s effective area (Aartsen et al. 2020; Abbasi et al. 2021b). This matches our observation. However, there are many different scenarios that agree with this work. In these cases, different source populations or states produce different neutrino spectra compared to one continuous power law. Another possible scenario including a source population emitting single power laws is described in Abbasi et al. (2023b). Our result agrees with the high-density scenario presented in Section 6 of Abbasi et al. (2023b). There, a high-density source population with low individual fluxes (with an

$E^{-2.5}$ energy spectrum) is the origin of alert events. Due to the sheer number of sources, we would be able to detect flux fluctuations in high energies as alert events without a detectable lower-energy component. In lower energies, the flux would be too low to be detected, and it would require a simultaneous fluctuation in both lower and higher energies such that both components could be detected from the same object.

3.2. Transient Sources

In our search for transient sources, we look for the most significant transient neutrino emission. Out of all 122 investigated alert+ origins, the most significant transient emission is the neutrino flare with the seed alert IceCube-170922A, which is associated with the blazar TXS 0506+056. Our search yields a local p -value of 0.14% (or a significance of 3σ). The main differences between the search in Aartsen et al. (2018b) and this work are as follows.

1. We have no external trigger in this work, whereas Aartsen et al. (2018b) were triggered by the observation of a flaring blazar.
2. We use 11 yr of recalibrated IceCube muon data, improving directional and energy reconstruction. For a discussion of how the contributing events are affected, see Appendix B.
3. We include a fit for the best source position and use expectation maximization to identify the time of the neutrino flare.

The corresponding flare is centered around a mean flare time $\hat{t}_T = 57001_{-26}^{+38}$ MJD and has a width of $\hat{\sigma}_T = 64_{-10}^{+35}$ days. These properties agree with Aartsen et al. (2018b), as shown in Figure 3. When correcting for the look-elsewhere effect, the global p -value is $p_{\text{global}} = 0.156$, which is not significant. Such a trial correction does not apply for the search reported in Aartsen et al. (2018b). Table 5 lists all results for the investigated regions.

The best-fit parameter can yield insight into the source emission. However, as mentioned in Section 2 and

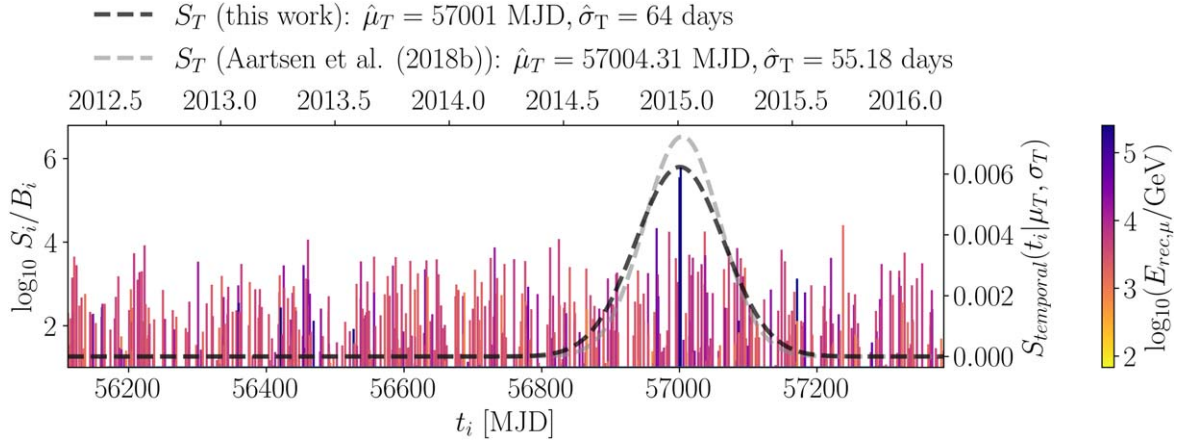


Figure 3. Logarithm of the signal-over-background ratio, $\log_{10} S_i/B_i$, distribution of individual events, i , vs. their detection time, t_i , between 2012 and 2016. The $\log_{10} S_i/B_i$ values are for the best-fit position (close to TXS 0506+056) and the best-fit spectral index. The color indicates the reconstructed muon energy, $E_{\text{rec},\mu}$, increasing from light to dark. The black dashed line shows this work's best-fit time pdf S_T (with the y-axis on the right). It agrees with the gray dashed pdf of Aartsen et al. (2018b).

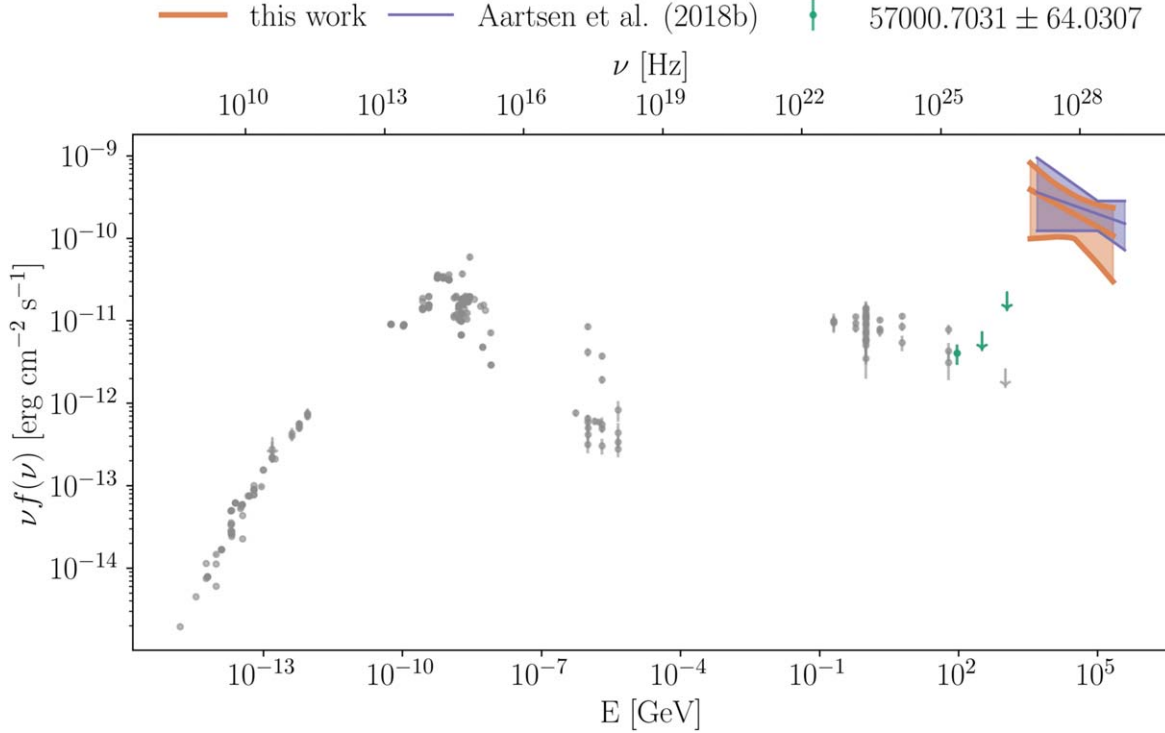


Figure 4. Spectral energy distribution of TXS 0506+056 in photons (gray dots) and neutrinos during the time of the neutrino flare (bands). The green dots (arrows) show gamma-ray emission (upper limits) during the time window of the neutrino flare detected by Fermi-LAT (Ackermann et al. 2012). This work's all-flavor neutrino flux during the flare (orange band; $3 \times \Phi_{100 \text{ TeV}}^{\nu_\mu + \bar{\nu}_\mu}$) agrees with the all-flavor flux given in White & Becker (1992); Wright et al. (1994, 2010); Gregory et al. (1996); Condon et al. (1998); Voges et al. (1999); Data for the photon SED are from Myers et al. (2003); Healey et al. (2007); Jackson et al. (2007); Nieppola et al. (2007); Abdo et al. (2010); Planck Collaboration et al. (2011, 2014, 2016); Bianchi et al. (2011); Bartoli et al. (2013); D'Elia et al. (2013); Evans et al. (2014); Boller et al. (2016); Nolan et al. (2012); Acero et al. (2015); Aartsen et al. (2018b; dark purple band). Giommi et al. (2018).

Appendix A, the best-fit results and the resulting flux estimations are biased. The best-fit result of the number of neutrinos in the neutrino flare is $\hat{n}_S = 12_{-7}^{+9}$ with a spectral index of $\hat{\gamma} = 2.3 \pm 0.4$. This corresponds to an average flux of $\Phi_{100 \text{ TeV}}^{\nu_\mu + \bar{\nu}_\mu} = 1.1_{-0.8}^{+0.9} \times 10^{-15} \text{ (TeV cm}^2 \text{ s)}^{-1}$ in the energy range of 3.5–213 TeV during the period of the neutrino flare. The corresponding single-flavor neutrino and antineutrino fluence, the flux integrated over the flaring period ($\hat{\mu}_T - 2\hat{\sigma}_T$ to $\hat{\mu}_T + 2\hat{\sigma}_T$), is $J_{100 \text{ TeV}}^{\nu_\mu + \bar{\nu}_\mu} = 1.2_{-0.8}^{+1.0} \times 10^{-8} \text{ (TeV cm}^2 \text{ s)}^{-1}$. This flux estimation also agrees with Aartsen et al. (2018b), as shown by the all-flavor neutrino flux (three times $\Phi_{100 \text{ TeV}}^{\nu_\mu + \bar{\nu}_\mu}$) in

Figure 4. In Appendix B, we compare the events contributing to the neutrino flare in this analysis and previous works and explain why the errors differ.

For transient emission, the lack of additional lower-energy neutrino emission (besides the reported local evidence associated with TXS 0506+056) can imply various scenarios. One is that neutrino flares occur rarely or might not necessarily be connected to the production sites of high-energy neutrinos. Similar to Section 3.1, it could also indicate that these neutrino sources emit a very hard energy spectrum, for example, with $\gamma \leq 1$.

4. Conclusion

Our study focused on the origin of IceCube’s highest-energy events, or alert+ events, to identify potential sources of additional neutrino emission. To achieve this, we systematically scanned the 90% uncertainty contours of reconstructed alert+ events with a resolution of 0.2° to determine the most significant source position. We assumed that the emission followed a power-law distribution, $\propto E^{-\gamma}$, with γ ranging from 1.5 to 4.

Our analysis found no evidence for continuous emission from a single source, as the data were consistent with the background assumption. Therefore, we placed a constraint on the overall combined flux from all positions, which was found to be 1.6% of the diffuse astrophysical neutrino flux observed by IceCube (for $\gamma=2$). If we included the alert+ events in the analysis, we could constrain all expected emissions from their respective directions to no more than 4.5% of the diffuse astrophysical neutrino flux (for $\gamma=2$). For a source spectral index similar to the diffuse astrophysical neutrino flux ($\gamma=2.37$), we constrain the overall combined flux to be less than 1.5% (excluding the alert+ events) and less than 8% (including the alert+ events) of the diffuse astrophysical neutrino flux. This indicates that different source populations or states produce different neutrino spectra compared to one continuous power law.

Our investigation confirmed the neutrino flare associated with the blazar TXS 0506+056 as the most significant transient emission from all investigated positions, with a local significance of about 3σ . When we corrected for the look-elsewhere effect in this analysis, the global significance was 15.6%, consistent with the background expectation. The parameters of the neutrino flare in this study using recalibrated data agreed with previously published results. We identified a Gaussian time window with a center at 57001_{-26}^{+38} MJD and a width of 64_{-10}^{+35} days as the best fit and estimated that 12_{-6}^{+9} neutrinos were detected during the flare with a best-fit spectral index of $\hat{\gamma} = 2.3 \pm 0.4$. This corresponds to a single-flavor neutrino fluence of $J_{100\text{ TeV}}^{\nu_\mu+\nu_\tau} = 1.2_{-0.8}^{+1.0} \times 10^{-8}$ (TeV cm²)⁻¹ and an average flux of $\Phi_{100\text{ TeV}}^{\nu_\mu+\nu_\tau} = 1.1_{-0.8}^{+0.9} \times 10^{-15}$ (TeV cm² s)⁻¹ during the $2\sigma_T$ time window. However, we find no other alert+ event with a similar local significance. TXS 0506+056 remains the only source candidate where we find the connection of a high-energy alert and a lower-energetic neutrino emission.

For neither continuous nor transient emission did we find evidence of a lower-energy neutrino component. This can be explained in various scenarios. One is a hard neutrino spectrum with $\gamma \leq 1$. In such a scenario, atmospheric background noise would dominate the lower-energy range, while the higher-energy range would yield single high-energy events. It could also be caused by a high-density source population as investigated in Abbasi et al. (2023b), where high-energy events are the result of fluctuations from a large population of sources with individually weak fluxes. In this case, the lower-energy flux would still be too low to be detected. Our finding also suggests that neutrino flares may be rare or produced at different sites than IceCube alert+ events or that there are sources mainly emitting high-energy neutrinos.

Acknowledgments

The IceCube Collaboration acknowledges significant contributions to this manuscript from Martina Karl. The authors gratefully acknowledge the support from the following agencies and institutions: USA—U.S. National Science Foundation Office of

Polar Programs, U.S. National Science Foundation Physics Division, U.S. National Science Foundation EPSCoR, U.S. National Science Foundation Office of Advanced Cyberinfrastructure, Wisconsin Alumni Research Foundation, Center for High Throughput Computing (CHTC) at the University of Wisconsin–Madison, Open Science Grid (OSG), Partnership to Advance Throughput Computing (PATH), Advanced Cyberinfrastructure Coordination Ecosystem: Services & Support (ACCESS), Frontera computing project at the Texas Advanced Computing Center, U.S. Department of Energy National Energy Research Scientific Computing Center, particle astrophysics research computing center at the University of Maryland, Institute for Cyber-Enabled Research at Michigan State University, astroparticle physics computational facility at Marquette University, NVIDIA Corporation, and Google Cloud Platform; Belgium—Funds for Scientific Research (FRS-FNRS and FWO), FWO Odysseus and Big Science programs, and Belgian Federal Science Policy Office (Belspo); Germany—Bundesministerium für Bildung und Forschung (BMBF), Deutsche Forschungsgemeinschaft (DFG), Helmholtz Alliance for Astroparticle Physics (HAP), Initiative and Networking Fund of the Helmholtz Association, Deutsches Elektronen Synchrotron (DESY), and High Performance Computing cluster of the RWTH Aachen; Sweden—Swedish Research Council, Swedish Polar Research Secretariat, Swedish National Infrastructure for Computing (SNIC), and Knut and Alice Wallenberg Foundation; European Union—EGI Advanced Computing for Research; Australia—Australian Research Council; Canada—Natural Sciences and Engineering Research Council of Canada, Calcul Québec, Compute Ontario, Canada Foundation for Innovation, WestGrid, and Digital Research Alliance of Canada; Denmark—Villum Fonden, Carlsberg Foundation, and European Commission; New Zealand—Marsden Fund; Japan—Japan Society for Promotion of Science (JSPS) and Institute for Global Prominent Research (IGPR) of Chiba University; Korea—National Research Foundation of Korea (NRF); Switzerland—Swiss National Science Foundation (SNSF).

Appendix A Parameter Recovery

When testing the method, as described in Section 2, with Monte Carlo simulations (Karl 2022), the best-fit number of signal neutrinos, n_S , and source spectral index, γ , show a bias compared to the true simulated source properties. For sources with simulated hard spectral indices (i.e., $\gamma=2$), there is a tendency to fit slightly softer spectra and a slightly larger number of signal neutrinos. For example, simulating an average of 10 neutrinos with $\gamma=2$ results in a mean best fit of $\hat{n}_S = 16$ and $\hat{\gamma} = 2.25$. For simulated sources following softer spectral indices (i.e., $\gamma=3$), the tendency is reversed to fitting slightly harder spectral indices and smaller numbers of signal neutrinos.

Several aspects influence this bias. One is a simplified spatial distribution in the form of a Rayleigh distribution (see Equation (3)). This is corrected using a kernel density estimation (KDE) approach, for example, in Abbasi et al. (2022a). However, the KDE approach is, so far, only feasible in the northern sky. Since we also search for neutrino sources from the southern sky, we chose the simplified method. Another aspect is that weak sources emitting only a few neutrinos are not always found during the position scan, since background fluctuations can dominate these weak sources. For example, for a continuous emission over 11 yr, the mean distance between the best-fit source position and the actual

simulated source is smaller than 0.3 for a flux resulting in five signal neutrinos on average. This also means that the best-fit n_S will be larger than 0 in many cases with no neutrino source, since the algorithm will find the position with the largest background fluctuation. Hence, correcting this bias is not straightforward, and this analysis is mainly sensitive to strong neutrino sources.

For transient sources, the bias is smaller. In the same example as above, 10 neutrinos with $\gamma=2$ emitted over a period of $\sigma_T \approx 55$ days are a much stronger signal compared to 10 neutrinos over 11 yr. Hence in this specific case, the mean best-fit $\hat{n}_S = 12$ and the best-fit $\hat{\gamma} = 2.1$. However, we still face the case that background fluctuations can dominate weak neutrino emission (in the case of $\sigma_T \approx 55$ days, anything below five neutrinos is difficult), which makes correcting this bias challenging. We have decided not to include an at best incomplete correction in this work. For now, measurements of point-source fluxes are only possible with the KDE approach.

Appendix B Transient Sources Analysis

Figure 5 shows the p -value map of the scanned region around IceCube-170922A on the left. The most significant

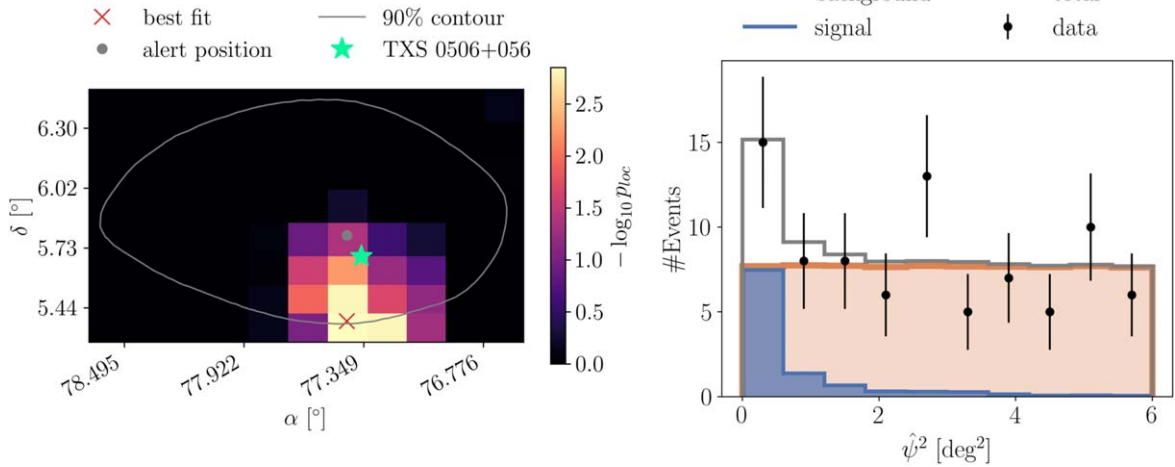


Figure 5. Left: p -value map of the alert region of IceCube-170922A. The gray dot indicates the reconstructed direction of IceCube-170922A, and the gray contour shows the 90% uncertainties of the reconstruction. The red cross marks the best-fit position of the position scan (0.6 from the reconstructed alert position). The star shows the location of TXS 0506+056. All black bins have p -values close to 1. Right: number of events at binned squared angular distances, $\hat{\psi}^2$, between TXS 0506+056 and the reconstructed event directions during the neutrino flare ($57001 \text{ MJD} \pm 2 \times 64$ days). Scrambled data in R.A. provide the background (blue), and Monte Carlo simulations for the best-fit flux ($n_S = 12$ and $\gamma = 2.31$) yield the signal (orange). The gray line combines the background with the signal and matches the data points (black). The data are shown with 68% uncertainties.

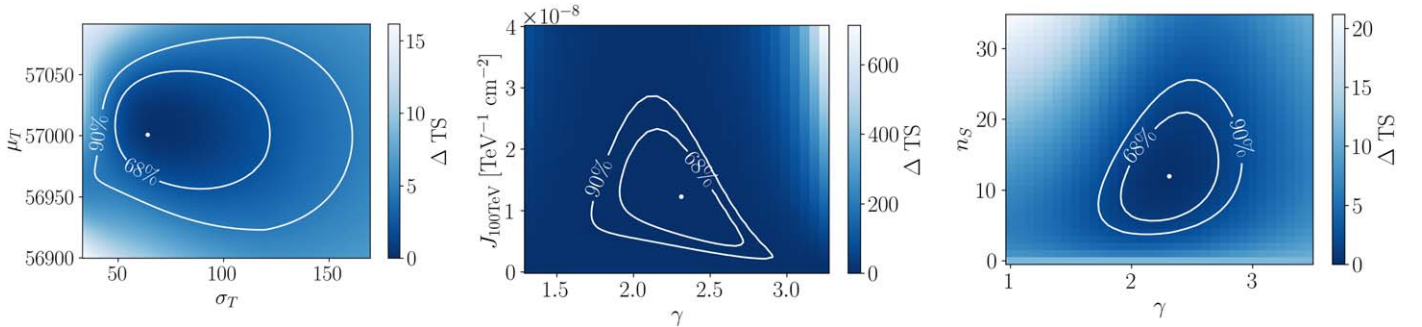


Figure 6. Change of the TS value for the different likelihood parameters. Left: profiled change for different μ_T and σ_T . n_S and γ are optimized at each step. The 68% uncertainties are $\hat{\mu}_T = 57001_{-26}^{+38}$ MJD and $\hat{\sigma}_T = 64_{-10}^{+35}$ days. Center: change when varying the signal fluence $J_{100 \text{ TeV}}^{\nu_\mu + \bar{\nu}_\mu}(n_S, \gamma)$. The 68% uncertainties on the fluence are $J_{100 \text{ TeV}}^{\nu_\mu + \bar{\nu}_\mu} = 1.2_{-0.8}^{+1.0} \times 10^{-8} (\text{TeV cm}^2)^{-1}$. Right: variation when changing n_S and γ . The 68% uncertainties are $\hat{n}_S = 12_{-7}^{+9}$ and $\hat{\gamma} = 2.3 \pm 0.4$.

position is within 0.5 from TXS 0506+056. The right panel of Figure 5 shows a histogram of the angular distance of events from TXS 0506+056. There is a clustering of events around the source position. The signal events for this plot are simulated according to the best-fit result of the likelihood ratio test ($\hat{n}_S = 12$, $\hat{\gamma} = 2.3$). The background distribution is scrambled data in R.A. The signal on top of the background flux matches the observed data.

To determine the uncertainties of the best-fit values, we run a likelihood scan over the parameter space and use Wilk's theorem (Wilks 1938) to determine the 68% and 90% contours (see Figure 6). These contours are relevant for the two-dimensional uncertainties of the flux as in Figure 4. For the time, we determine the profiled change of the TS for different μ_T and σ_T . The best n_S and γ are fitted for each value. The 68% uncertainties determined by a profiled change of the TS are $\hat{\mu}_T = 57001_{-26}^{+38}$ MJD and $\hat{\sigma}_T = 64_{-10}^{+35}$ days. The one-dimensional errors for fluence, number of signal neutrinos n_S , and spectral index γ are determined with the profiled change of the TS where the mean flaring time and the flare width are kept fixed to the best-fit values. For the signal fluence, the 68% uncertainties are $J_{100 \text{ TeV}}^{\nu_\mu + \bar{\nu}_\mu} = 1.2_{-0.8}^{+1.0} \times 10^{-8} (\text{TeV cm}^2)^{-1}$, and for n_S and γ , we get $\hat{n}_S = 12_{-7}^{+9}$ and $\hat{\gamma} = 2.3 \pm 0.4$.

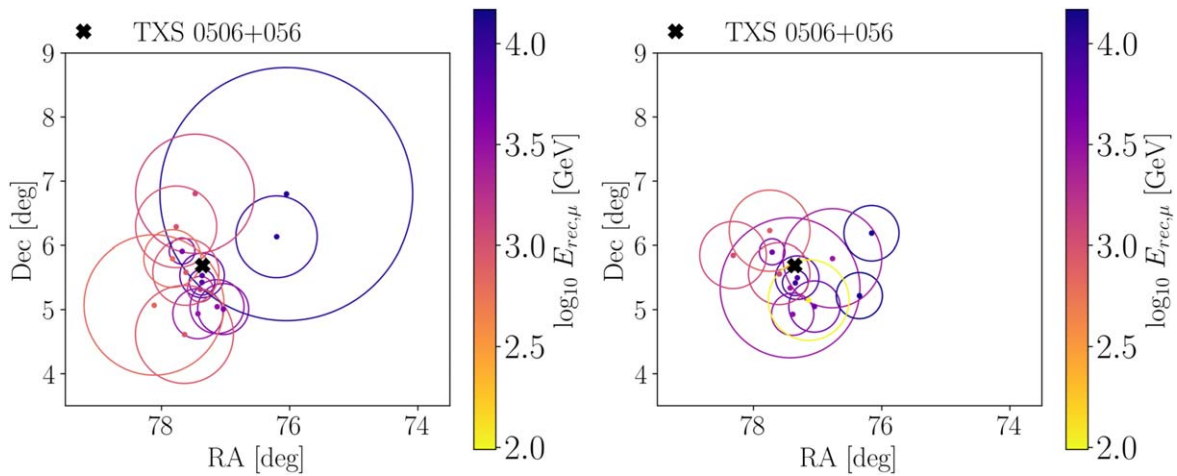


Figure 7. Position and energy (color) of the 14 events contributing the most to the TXS 0506+056 neutrino flare. The circles show the uncertainty of the directional reconstruction, σ . Left: the 14 most contributing events from the data sample used in this work (see Table 2). Right: the 14 most contributing events from the old data sample (Abbasi et al. 2021b).

Table 2
Comparison of the Top 14 Events Contributing to the Neutrino Flare of TXS 0506+056 in Different Data Sets

| MJD | This Work | | | | Abbasi et al. (2021b) | | | | Ranking |
|------------|------------|-------------|----------------|---------------------------|-----------------------|-------------|----------------|---------------------------|---------|
| | R.A. (deg) | Decl. (deg) | σ (deg) | $\log_{10}(E/\text{GeV})$ | R.A. (deg) | Decl. (deg) | σ (deg) | $\log_{10}(E/\text{GeV})$ | |
| 56940.9084 | 77.36 | 5.42 | 0.20 | 3.81 | 77.35 | 5.42 | 0.20 | 3.97 | 1 |
| 57009.5301 | 77.36 | 5.53 | 0.34 | 3.85 | 77.32 | 5.50 | 0.34 | 3.91 | 2 |
| 56973.3971 | 77.03 | 5.01 | 0.39 | 3.61 | 77.05 | 5.05 | 0.40 | 3.71 | 12 |
| 57112.6530 | 77.39 | 5.32 | 0.20 | 3.23 | 77.43 | 5.34 | 1.09 | 3.46 | 7 |
| 57072.2088 | 77.13 | 5.04 | 0.42 | 3.50 | 76.35 | 5.22 | 0.36 | 3.43 | 9 |
| 56981.1313 | 76.20 | 6.13 | 0.63 | 4.03 | 76.16 | 6.19 | 0.43 | 4.13 | 5 |
| 57089.4395 | 77.67 | 5.91 | 0.20 | 3.62 | 77.71 | 5.90 | 0.20 | 3.69 | 3 |
| 56927.8601 | 77.43 | 4.93 | 0.39 | 3.46 | 77.39 | 4.93 | 0.33 | 3.53 | 13 |
| 56955.7917 | 77.61 | 5.58 | 0.51 | 2.99 | 77.60 | 5.56 | 0.48 | 3.09 | 6 |
| 57072.9895 | 76.05 | 6.80 | 1.97 | 4.09 | 76.35 | 5.22 | 0.36 | 4.17 | 4 |
| 56940.5215 | 77.82 | 5.79 | 0.44 | 2.80 | ... | ... | ... | ... | ... |
| 57031.8224 | 77.64 | 4.61 | 0.76 | 2.96 | ... | ... | ... | ... | ... |
| 56937.8189 | 77.77 | 6.29 | 0.63 | 2.98 | 77.75 | 6.23 | 0.63 | 2.91 | 11 |
| 56983.2476 | 77.47 | 6.80 | 0.92 | 3.09 | ... | ... | ... | ... | ... |

Note. Left: Top 14 events with the strongest contribution to the neutrino flare of TXS 0506+056, sorted by significance. Right: The same events in the data sample published in Abbasi et al. (2021b). The last column states the ranking of the contribution in previous analyses. The data set used in this work has improved directional and energy reconstruction. Some events have shifted in position and have slightly different energies.

Table 2 lists the top 14 events contributing to the neutrino flare, sorted by their S_i/B_i value multiplied by S_T . We compare this with a previous data sample (Abbasi et al. 2021b; for events also included in that sample) to emphasize how the updated photomultiplier calibration affects the reconstructed direction, angular error, and energy.

The improved directional and energy reconstruction has changed the contributing events compared to previous analyses (Aartsen et al. 2018b; Abbasi et al. 2021b). Most of the significance is caused by the two most contributing events, which remain the same (see also Karl 2022). However, their position is shifted, and their energy is changed. For the remaining events, the contributing order has changed, or the events themselves differ. Figure 7 shows the position and energy of the 14 events contributing the most to the neutrino flare from the previous data set (left) and the improved data used in this work (right). The event with the largest error region

($\sigma = 1^\circ 9$) in the right panel is also included in the left panel. However, the uncertainty was underestimated in the previous data sample ($\sigma = 0^\circ 36$), and its position has shifted.

Appendix C IceCube Alert+ Events

Table 3 lists all alert+ events used in this work. The selection aims for a high signal purity and comprises alerts published in the gold alert channel (Abbasi et al. 2023a). Additionally, we include high-energy events from Abbasi et al. (2022b) that were classified to be of likely astrophysical origin by a new event classifier (Kronmueller & Glauch 2019). We excluded events within 30° of the geographic poles and events with uncertainties $\geq 100 \text{ deg}^2$. The final selection has a probability of being astrophysical of > 0.5 . We remove the respective alert+ event from IceCube data when running the analysis.

Table 3
Alert+ Events Investigated in This Work

| Index | Track Name | Time (MJD) | R.A. (deg) | Decl. (deg) |
|-------|------------|------------|--|--|
| 1 | DIF090813 | 55056.6983 | 29.51 ^{+0.40} _{-0.38} | 1.23 ^{+0.18} _{-0.22} |
| 2 | DIF091106 | 55141.1275 | 298.21 ^{+0.53} _{-0.57} | 11.74 ^{+0.32} _{-0.38} |
| 3 | DIF100608 | 55355.4872 | 344.93 ^{+3.39} _{-2.90} | 23.58 ^{+2.31} _{-4.13} |
| 4 | DIF100623 | 55370.7355 | 141.25 ^{+0.46} _{-0.45} | 47.80 ^{+0.56} _{-0.48} |
| 5 | DIF100710 | 55387.5362 | 306.96 ^{+2.70} _{-2.28} | 21.00 ^{+2.25} _{-1.56} |
| 6 | DIF100925 | 55464.8959 | 266.29 ^{+0.58} _{-0.63} | 13.40 ^{+0.23} _{-0.45} |
| 7 | DIF101009 | 55478.3806 | 331.09 ^{+0.56} _{-0.72} | 11.10 ^{+0.48} _{-0.58} |
| 8 | DIF101028 | 55497.3033 | 88.68 ^{+0.54} _{-0.55} | 0.46 ^{+0.33} _{-0.27} |
| 9 | HESE101112 | 55512.5516 | 110.56 ^{+0.80} _{-0.37} | -0.37 ^{+0.48} _{-0.65} |
| 10 | DIF101113 | 55513.5995 | 285.95 ^{+1.29} _{-1.50} | 3.15 ^{+0.70} _{-0.63} |
| 11 | DIF110128 | 55589.5628 | 307.53 ^{+0.82} _{-0.81} | 1.19 ^{+0.35} _{-0.32} |
| 12 | EHE110304 | 55624.9548 | 116.37 ^{+0.73} _{-0.73} | -10.72 ^{+0.57} _{-0.65} |
| 13 | IC110514A | 55695.0642 | 138.47 ^{+6.68} _{-3.78} | -1.94 ^{+0.97} _{-1.12} |
| 14 | DIF110521 | 55702.7666 | 235.13 ^{+2.70} _{-1.76} | 20.30 ^{+1.00} _{-1.43} |
| 15 | IC110610A | 55722.4261 | 272.55 ^{+1.67} _{-2.42} | 35.64 ^{+1.30} _{-1.05} |
| 16 | IC110714A | 55756.1130 | 68.20 ^{+0.31} _{-1.10} | 40.67 ^{+0.44} _{-0.44} |
| 17 | DIF110722 | 55764.2196 | 315.66 ^{+5.91} _{-5.35} | 5.29 ^{+4.85} _{-4.72} |
| 18 | IC110902A | 55806.0922 | 9.76 ^{+2.85} _{-1.32} | 7.59 ^{+0.87} _{-0.86} |
| 19 | IC110907A | 55811.7946 | 196.08 ^{+3.92} _{-2.68} | 9.40 ^{+1.56} _{-1.05} |
| 20 | DIF110930 | 55834.4451 | 266.48 ^{+2.09} _{-1.55} | -4.41 ^{+0.59} _{-0.86} |
| 21 | DIF111201 | 55896.8575 | 222.87 ^{+1.95} _{-7.73} | 1.87 ^{+1.25} _{-1.18} |
| 22 | IC111216A | 55911.2769 | 36.74 ^{+1.80} _{-2.24} | 18.88 ^{+2.46} _{-2.82} |
| 23 | IC120301A | 55987.8069 | 237.96 ^{+0.53} _{-0.61} | 18.76 ^{+0.47} _{-0.51} |
| 24 | IC120515A | 56062.9590 | 198.94 ^{+1.71} _{-1.41} | 32.00 ^{+0.97} _{-1.09} |
| 25 | IC120523A | 56070.5743 | 171.08 ^{+0.66} _{-1.41} | 26.44 ^{+0.46} _{-0.37} |
| 26 | IC120807A | 56146.2071 | 330.07 ^{+0.84} _{-0.83} | 1.42 ^{+0.59} _{-0.45} |
| 27 | IC120916A | 56186.3053 | 182.24 ^{+1.36} _{-1.71} | 3.88 ^{+0.68} _{-0.82} |
| 28 | IC120922A | 56192.5493 | 70.62 ^{+1.49} _{-1.27} | 19.79 ^{+0.91} _{-0.71} |
| 29 | IC121011A | 56211.7709 | 205.14 ^{+0.66} _{-0.71} | -2.28 ^{+0.53} _{-0.56} |
| 30 | IC121026A | 56226.5995 | 169.80 ^{+1.32} _{-1.40} | 27.91 ^{+0.85} _{-0.88} |
| 31 | IC130127A | 56319.2800 | 352.97 ^{+1.32} _{-1.01} | -1.98 ^{+0.97} _{-0.89} |
| 32 | IC130408A | 56390.1888 | 167.83 ^{+2.63} _{-3.96} | 20.66 ^{+1.28} _{-0.99} |
| 33 | IC130627A | 56470.1104 | 93.74 ^{+1.01} _{-1.15} | 14.17 ^{+1.23} _{-1.04} |
| 34 | DIF130817 | 56521.8320 | 224.89 ^{+0.87} _{-1.19} | -4.44 ^{+1.21} _{-0.94} |
| 35 | IC130907A | 56542.7931 | 130.17 ^{+0.48} _{-0.31} | -10.54 ^{+0.26} _{-0.30} |
| 36 | IC131014A | 56579.9092 | 32.92 ^{+0.87} _{-0.71} | 10.28 ^{+0.41} _{-0.57} |
| 37 | IC131023A | 56588.5585 | 301.90 ^{+1.02} _{-1.05} | 11.61 ^{+1.14} _{-1.30} |
| 38 | IC131124A | 56620.1451 | 285.16 ^{+2.20} _{-1.54} | 19.47 ^{+1.43} _{-1.46} |
| 39 | IC131204A | 56630.4701 | 288.98 ^{+1.10} _{-0.83} | -14.21 ^{+0.77} _{-1.21} |
| 40 | IC140101A | 56658.4039 | 192.26 ^{+2.07} _{-2.37} | -2.69 ^{+1.01} _{-0.71} |
| 41 | IC140108A | 56665.3079 | 344.66 ^{+0.53} _{-0.48} | 1.57 ^{+0.37} _{-0.34} |
| 42 | IC140109A | 56666.5030 | 293.12 ^{+0.79} _{-1.19} | 33.02 ^{+0.45} _{-0.53} |
| 43 | IC140203A | 56691.7851 | 349.58 ^{+2.64} _{-2.54} | -13.55 ^{+1.14} _{-1.74} |
| 44 | DIF140522 | 56799.9614 | 349.39 ^{+2.89} _{-4.12} | 18.05 ^{+1.94} _{-1.80} |
| 45 | IC140609A | 56817.6364 | 106.26 ^{+2.68} _{-2.15} | 1.31 ^{+1.04} _{-0.86} |
| 46 | IC140611A | 56819.2044 | 110.65 ^{+0.53} _{-0.61} | 11.45 ^{+0.19} _{-0.19} |
| 47 | IC140705A | 56843.6687 | 25.88 ^{+1.85} _{-2.98} | 2.54 ^{+0.79} _{-1.76} |
| 48 | IC140923A | 56923.7211 | 169.72 ^{+0.70} _{-0.84} | -1.60 ^{+0.52} _{-0.30} |
| 49 | IC140927A | 56927.1608 | 50.89 ^{+3.91} _{-5.14} | -0.63 ^{+1.49} _{-1.42} |
| 50 | IC150127A | 57049.4813 | 100.37 ^{+1.36} _{-1.62} | 4.59 ^{+0.79} _{-0.67} |
| 51 | IC150515A | 57157.9416 | 91.49 ^{+0.93} _{-0.74} | 12.14 ^{+0.53} _{-0.50} |
| 52 | IC150714A | 57217.9097 | 326.29 ^{+1.50} _{-1.31} | 26.36 ^{+1.89} _{-2.19} |
| 53 | IC150812B | 57246.7591 | 328.27 ^{+0.75} _{-0.88} | 6.17 ^{+0.48} _{-0.53} |
| 54 | IC150831A | 57265.2178 | 54.76 ^{+0.92} _{-0.93} | 34.00 ^{+1.14} _{-1.20} |
| 55 | IC150904A | 57269.7597 | 133.77 ^{+0.53} _{-0.88} | 28.08 ^{+0.51} _{-0.55} |
| 56 | IC150919A | 57284.2057 | 279.54 ^{+1.75} _{-2.29} | 30.35 ^{+2.18} _{-1.51} |
| 57 | IC150923A | 57288.0268 | 103.23 ^{+0.70} _{-1.15} | 3.96 ^{+0.60} _{-0.75} |
| 58 | IC150926A | 57291.9012 | 194.55 ^{+0.79} _{-1.23} | -4.56 ^{+0.94} _{-0.63} |
| 59 | IC151017A | 57312.6757 | 197.53 ^{+2.47} _{-2.72} | 19.95 ^{+3.00} _{-2.29} |
| 60 | IC151114A | 57340.8735 | 76.16 ^{+1.36} _{-1.37} | 12.71 ^{+0.65} _{-0.72} |
| 61 | IC151122A | 57348.5316 | 262.05 ^{+0.87} _{-1.06} | -2.24 ^{+0.64} _{-0.67} |
| 62 | IC160104A | 57391.4438 | 79.41 ^{+0.83} _{-0.75} | 5.00 ^{+0.87} _{-0.97} |
| 63 | IC160128A | 57415.1835 | 263.76 ^{+1.10} _{-1.80} | -14.90 ^{+1.08} _{-1.20} |
| 64 | IC160225A | 57443.8804 | 311.87 ^{+2.19} _{-1.77} | 60.06 ^{+1.65} _{-1.38} |
| 65 | IC160331A | 57478.5652 | 151.22 ^{+0.66} _{-0.66} | 15.48 ^{+0.66} _{-0.73} |
| 66 | IC160510A | 57518.6640 | 352.88 ^{+1.76} _{-1.45} | 1.90 ^{+0.75} _{-0.67} |

Table 3
(Continued)

| Index | Track Name | Time (MJD) | R.A. (deg) | Decl. (deg) |
|-------|------------|------------|--|--|
| 67 | EHE160731 | 57600.0799 | 214.50 ^{+0.75} _{-0.75} | -0.33 ^{+0.75} _{-0.75} |
| 68 | IC160806A | 57606.5150 | 122.78 ^{+0.88} _{-1.23} | -0.71 ^{+0.56} _{-0.56} |
| 69 | IC160814A | 57614.9069 | 200.04 ^{+3.12} _{-2.68} | -32.13 ^{+1.74} _{-1.25} |
| 70 | IC160924A | 57655.7411 | 241.13 ^{+4.92} _{-5.89} | 1.34 ^{+3.40} _{-2.79} |
| 71 | IC161001A | 57662.4392 | 192.57 ^{+2.50} _{-2.07} | 37.12 ^{+1.51} _{-2.48} |
| 72 | DIF161011 | 57672.0796 | 26.38 ^{+0.66} _{-0.66} | 9.55 ^{+0.66} _{-0.66} |
| 73 | IC161012A | 57673.6126 | 190.06 ^{+2.20} _{-4.04} | -7.48 ^{+2.18} _{-2.98} |
| 74 | IC161117A | 57709.3320 | 78.66 ^{+1.85} _{-1.93} | 1.60 ^{+1.91} _{-1.79} |
| 75 | IC161210A | 57732.8380 | 46.36 ^{+2.38} _{-0.92} | 15.25 ^{+0.93} _{-1.08} |
| 76 | IC170105A | 57758.1419 | 309.95 ^{+5.01} _{-7.56} | 8.16 ^{+2.00} _{-3.34} |
| 77 | IC170321A | 57833.3141 | 98.26 ^{+1.32} _{-0.92} | -15.06 ^{+1.04} _{-1.20} |
| 78 | IC170514B | 57887.3002 | 227.37 ^{+1.23} _{-1.10} | 30.65 ^{+1.40} _{-0.67} |
| 79 | IC170626A | 57930.5193 | 280.99 ^{+3.03} _{-1.63} | 8.80 ^{+1.13} _{-0.90} |
| 80 | IC170704A | 57938.2926 | 230.45 ^{+1.67} _{-1.71} | 23.36 ^{+1.10} _{-0.89} |
| 81 | IC170717A | 57951.8177 | 208.39 ^{+1.41} _{-1.19} | 25.16 ^{+1.41} _{-1.35} |
| 82 | IC170803A | 57968.0838 | 1.10 ^{+4.48} _{-1.76} | 4.63 ^{+0.41} _{-0.41} |
| 83 | IC170809A | 57974.5971 | 21.27 ^{+1.75} _{-1.06} | -2.28 ^{+0.60} _{-0.67} |
| 84 | IC170824A | 57989.5538 | 41.92 ^{+3.04} _{-3.56} | 12.37 ^{+1.45} _{-1.30} |
| 85 | IC170922A | 58018.8712 | 77.43 ^{+1.14} _{-0.75} | 5.79 ^{+0.64} _{-0.41} |
| 86 | IC170923A | 58019.0213 | 173.45 ^{+2.38} _{-2.55} | -2.54 ^{+0.90} _{-1.30} |
| 87 | IC171015A | 58041.0656 | 162.91 ^{+2.98} _{-1.72} | -15.48 ^{+1.62} _{-1.99} |
| 88 | IC171106A | 58063.7775 | 340.14 ^{+0.61} _{-0.62} | 7.44 ^{+0.31} _{-0.26} |
| 89 | IC180123A | 58141.6771 | 77.12 ^{+2.51} _{-2.90} | 8.01 ^{+0.41} _{-0.49} |
| 90 | IC180410A | 58218.7768 | 218.50 ^{+0.79} _{-1.28} | 0.56 ^{+0.75} _{-0.75} |
| 91 | IC180417A | 58225.2785 | 305.73 ^{+3.60} _{-1.58} | -4.41 ^{+0.68} _{-0.74} |
| 92 | IC180908A | 58369.8330 | 144.98 ^{+1.49} _{-2.20} | -2.39 ^{+1.16} _{-1.12} |
| 93 | IC181023A | 58414.6927 | 270.18 ^{+1.89} _{-1.72} | -8.42 ^{+1.13} _{-1.55} |
| 94 | IC181120A | 58442.7087 | 25.71 ^{+5.54} _{-5.28} | 11.72 ^{+2.41} _{-4.50} |
| 95 | IC181121A | 58443.5800 | 132.19 ^{+7.34} _{-6.99} | 32.93 ^{+4.19} _{-3.57} |
| 96 | IC190124A | 58507.1555 | 307.44 ^{+0.53} _{-1.14} | -32.22 ^{+0.96} _{-0.31} |
| 97 | IC190214A | 58528.6727 | 228.25 ^{+0.79} _{-0.53} | -4.14 ^{+0.37} _{-0.30} |
| 98 | IC190221A | 58535.3512 | 268.59 ^{+1.41} _{-1.58} | -17.00 ^{+1.25} _{-0.50} |
| 99 | IC190503A | 58606.7244 | 120.19 ^{+0.66} _{-0.66} | 6.43 ^{+0.68} _{-0.75} |
| 100 | IC190515A | 58618.4506 | 127.88 ^{+0.79} _{-0.83} | 12.60 ^{+0.49} _{-0.46} |
| 101 | IC190613A | 58647.8294 | 312.19 ^{+0.66} _{-0.79} | 26.57 ^{+0.75} _{-0.71} |
| 102 | IC190619A | 58653.5516 | 343.52 ^{+4.13} _{-3.16} | 10.28 ^{+2.01} _{-2.76} |
| 103 | IC190730A | 58694.8685 | 226.14 ^{+1.28} _{-1.97} | 10.77 ^{+1.03} _{-1.18} |
| 104 | IC190922A | 58748.4047 | 167.30 ^{+2.81} _{-2.72} | -22.27 ^{+3.39} _{-3.30} |
| 105 | IC190922B | 58748.9611 | 5.71 ^{+1.19} _{-1.27} | -1.53 ^{+0.90} _{-0.78} |
| 106 | IC191001A | 58757.8398 | 313.99 ^{+6.94} _{-5.49} | 12.79 ^{+1.65} _{-1.64} |
| 107 | IC191119A | 58806.0427 | 229.31 ^{+5.49} _{-4.97} | 3.77 ^{+2.47} _{-2.24} |
| 108 | IC200109A | 58857.9873 | 165.45 ^{+3.61} _{-4.39} | 11.80 ^{+1.18} _{-1.30} |
| 109 | IC200530A | 58999.3295 | 255.37 ^{+2.46} _{-2.55} | 26.61 ^{+2.32} _{-3.25} |
| 110 | IC200615A | 59015.6176 | 142.95 ^{+1.15} _{-1.40} | 3.66 ^{+1.16} _{-1.01} |
| 111 | IC200926A | 59118.3293 | 96.46 ^{+0.70} _{-0.53} | -4.33 ^{+0.60} _{-0.75} |
| 112 | IC200929A | 59121.7421 | 29.53 ^{+0.53} _{-0.53} | 3.47 ^{+0.71} _{-0.34} |
| 113 | IC201007A | 59129.9179 | 265.17 ^{+0.48} _{-0.49} | 5.34 ^{+0.30} _{-0.19} |
| 114 | IC201114A | 59167.6288 | 105.73 ^{+0.93} _{-1.27} | 5.87 ^{+1.01} _{-1.05} |
| 115 | IC201115A | 59168.0885 | 195.12 ^{+1.23} _{-1.45} | 1.38 ^{+1.27} _{-1.08} |
| 116 | IC201130A | 59183.8485 | 30.54 ^{+1.10} _{-1.27} | -12.10 ^{+1.14} _{-1.11} |
| 117 | IC201209A | 59192.4276 | 6.86 ^{+1.01} _{-1.19} | -9.25 ^{+0.94} _{-1.10} |
| 118 | IC201221A | 59204.5256 | 261.69 ^{+2.28} _{-2.46} | 41.81 ^{+1.25} _{-1.14} |
| 119 | IC201222A | 59205.0391 | 206.37 ^{+0.88} _{-0.75} | 13.44 ^{+0.54} _{-0.35} |
| 120 | IC210210A | 59255.4958 | 206.06 ^{+1.40} _{-0.95} | 4.78 ^{+0.62} _{-0.56} |
| 121 | IC210811A | 59437.0852 | 270.79 ^{+1.07} _{-1.08} | 25.28 ^{+0.79} _{-0.84} |
| 122 | IC210922A | 59479.7620 | 60.73 ^{+0.88} _{-0.61} | -4.18 ^{+0.37} _{-0.53} |

Note. All alert events (track name starting with “IC”) and high-energy tracks (track name starting with “DIF” (selected from Abbasi et al. 2022b)), “EHE” (extremely high-energy), or “HESE” (high-energy-starting event) investigated in this this work. The track name includes the time of detection in the format yymmdd. In the case of alert events, the letter “A” or “B” is used to distinguish events detected on the same day. The time is the detection time in MJD, and R.A. and decl. list the best reconstruction coordinates with 90% confidence level uncertainties.

Appendix D Results Tables

Table 4 presents the results of the time-integrated point-source search, sorted by local significance. We list the best-fit values of our analysis (position, mean number of signal events,

spectral index) and the 90% confidence level upper flux limits with their respective valid energy ranges. Table 5 shows the results of the time-dependent analysis (also sorted by local significance) and the best-fit values for position, mean number of signal events, spectral index, and the respective best-fit time window for a single flare.

Table 4
Results of the Individual Time-integrated Analysis Sorted by Significance

| Index | R.A. (deg) | Decl. (deg) | \hat{n}_S | $\hat{\gamma}$ | p_{local} | $\Phi_{90\%100 \text{ TeV}}$ (TeV cm ² s) ⁻¹ | $E_{\nu, \Phi, \text{min}}$ (TeV) | $E_{\nu, \Phi, \text{max}}$ (TeV) |
|-------|---------------|----------------|-------------|----------------|--------------------|---|--------------------------------------|--------------------------------------|
| 13 | 137.87 | -2.69 | 37.50 | 3.20 | 0.02 | 6.88×10^{-17} | 0.9 | 483.1 |
| 106 | 318.48 | 11.88 | 13.38 | 2.08 | 0.03 | 9.00×10^{-17} | 0.7 | 132.7 |
| 14 | 237.00 | 19.41 | 46.18 | 4.00 | 0.03 | 9.20×10^{-17} | 0.7 | 88.3 |
| 2 | 298.74 | 11.74 | 38.86 | 4.00 | 0.04 | 8.95×10^{-17} | 0.7 | 134.0 |
| 83 | 22.02 | -2.13 | 28.76 | 2.93 | 0.04 | 5.00×10^{-17} | 0.9 | 439.5 |
| 54 | 54.99 | 33.66 | 34.34 | 4.00 | 0.04 | 5.58×10^{-17} | 0.7 | 50.8 |
| 16 | 68.36 | 40.82 | 4.48 | 1.71 | 0.05 | 7.31×10^{-17} | 0.7 | 40.8 |
| 50 | 50.69 | -0.44 | 43.72 | 4.00 | 0.06 | 5.77×10^{-17} | 0.8 | 380.2 |
| 74 | 79.40 | 2.75 | 20.01 | 2.49 | 0.06 | 6.35×10^{-17} | 0.8 | 293.8 |
| 10 | 284.83 | 3.32 | 16.71 | 2.38 | 0.07 | 7.66×10^{-17} | 0.8 | 286.4 |
| 60 | 75.38 | 12.87 | 13.39 | 2.17 | 0.07 | 4.77×10^{-17} | 0.7 | 118.6 |
| 23 | 237.76 | 19.08 | 37.66 | 4.00 | 0.07 | 6.31×10^{-17} | 0.7 | 95.1 |
| 44 | 349.58 | -13.17 | 12.27 | 2.64 | 0.07 | 6.17×10^{-17} | 17.3 | 5093.3 |
| 25 | 171.74 | 26.44 | 11.18 | 2.31 | 0.07 | 6.01×10^{-17} | 0.7 | 67.3 |
| 72 | 26.38 | 9.55 | 9.84 | 2.13 | 0.08 | 2.15×10^{-16} | 0.8 | 158.1 |
| 45 | 350.01 | 19.02 | 40.34 | 3.91 | 0.10 | 7.68×10^{-17} | 0.7 | 101.2 |
| 40 | 190.68 | -2.35 | 26.39 | 4.00 | 0.11 | 4.11×10^{-17} | 0.9 | 462.4 |
| 90 | 218.32 | -0.15 | 32.53 | 3.49 | 0.11 | 4.22×10^{-17} | 0.8 | 368.1 |
| 11 | 307.86 | 1.36 | 11.50 | 2.42 | 0.14 | 3.24×10^{-17} | 0.8 | 353.2 |
| 93 | 269.42 | -7.48 | 15.52 | 2.95 | 0.15 | 8.71×10^{-17} | 2.2 | 2118.4 |
| 65 | 151.55 | 15.98 | 30.25 | 3.05 | 0.16 | 5.88×10^{-17} | 0.7 | 105.0 |
| 77 | 99.20 | -15.86 | 11.40 | 3.81 | 0.16 | 2.11×10^{-16} | 22.7 | 6823.4 |
| 84 | 43.34 | 12.18 | 40.03 | 3.49 | 0.16 | 7.54×10^{-17} | 0.7 | 131.2 |
| 85 | 77.43 | 5.38 | 16.73 | 2.54 | 0.17 | 4.18×10^{-17} | 0.8 | 237.1 |
| 99 | 120.35 | 6.05 | 24.65 | 2.81 | 0.20 | 4.68×10^{-17} | 0.8 | 223.4 |
| 55 | 133.77 | 27.71 | 22.04 | 4.00 | 0.20 | 3.85×10^{-17} | 0.7 | 64.4 |
| 120 | 206.26 | 4.41 | 26.47 | 2.89 | 0.20 | 3.79×10^{-17} | 0.8 | 265.5 |
| 4 | 141.25 | 47.32 | 17.24 | 2.61 | 0.21 | 7.67×10^{-17} | 0.7 | 32.4 |
| 9 | 111.36 | -0.37 | 25.89 | 4.00 | 0.21 | 2.89×10^{-17} | 0.8 | 371.5 |
| 81 | 208.19 | 25.69 | 5.14 | 1.86 | 0.22 | 5.56×10^{-17} | 0.7 | 65.9 |
| 28 | 70.62 | 19.43 | 8.08 | 2.09 | 0.22 | 4.92×10^{-17} | 0.7 | 86.5 |
| 15 | 273.27 | 36.20 | 22.40 | 2.72 | 0.22 | 6.14×10^{-17} | 0.7 | 43.9 |
| 30 | 171.12 | 27.73 | 32.96 | 3.94 | 0.23 | 5.37×10^{-17} | 0.7 | 62.2 |
| 31 | 353.91 | -1.20 | 20.58 | 2.65 | 0.24 | 3.11×10^{-17} | 0.9 | 394.5 |
| 18 | 9.38 | 7.59 | 5.54 | 2.09 | 0.24 | 4.38×10^{-17} | 0.8 | 181.1 |
| 115 | 194.76 | 2.47 | 17.33 | 2.48 | 0.26 | 2.81×10^{-17} | 0.8 | 300.6 |
| 33 | 93.74 | 14.17 | 18.68 | 2.58 | 0.26 | 3.76×10^{-17} | 0.7 | 116.7 |
| 113 | 265.17 | 5.15 | 21.84 | 4.00 | 0.28 | 4.00×10^{-17} | 0.8 | 248.3 |
| 47 | 27.54 | 2.74 | 36.77 | 3.79 | 0.28 | 3.52×10^{-17} | 0.8 | 293.8 |
| 34 | 225.59 | -4.09 | 14.38 | 2.78 | 0.30 | 3.24×10^{-17} | 1.0 | 642.7 |
| 119 | 206.90 | 13.27 | 20.54 | 3.16 | 0.30 | 3.12×10^{-17} | 0.7 | 118.6 |
| 112 | 29.35 | 3.30 | 22.47 | 3.12 | 0.30 | 3.70×10^{-17} | 0.8 | 281.2 |
| 114 | 104.46 | 6.38 | 28.34 | 3.01 | 0.30 | 2.82×10^{-17} | 0.8 | 224.4 |
| 94 | 26.90 | 7.81 | 47.41 | 4.00 | 0.30 | 7.00×10^{-17} | 0.8 | 170.6 |
| 7 | 330.73 | 11.10 | 21.11 | 2.90 | 0.31 | 3.57×10^{-17} | 0.7 | 134.0 |
| 56 | 277.48 | 29.41 | 25.41 | 2.83 | 0.32 | 2.86×10^{-17} | 0.7 | 55.0 |
| 75 | 46.95 | 15.99 | 32.99 | 3.15 | 0.32 | 4.65×10^{-17} | 0.7 | 106.7 |
| 59 | 195.23 | 20.14 | 8.95 | 2.09 | 0.33 | 6.66×10^{-17} | 0.7 | 83.0 |
| 79 | 283.21 | 9.37 | 32.19 | 3.43 | 0.33 | 5.19×10^{-17} | 0.8 | 167.1 |
| 78 | 227.78 | 30.25 | 28.65 | 4.00 | 0.33 | 6.23×10^{-17} | 0.7 | 54.3 |
| 122 | 60.27 | -3.99 | 6.55 | 4.00 | 0.34 | 5.41×10^{-17} | 1.0 | 619.4 |
| 52 | 91.86 | 12.32 | 23.31 | 3.25 | 0.34 | 3.58×10^{-17} | 0.7 | 130.0 |
| 86 | 171.49 | -2.36 | 8.32 | 2.19 | 0.34 | 3.72×10^{-17} | 0.9 | 467.7 |
| 49 | 168.88 | -1.43 | 20.41 | 4.00 | 0.35 | 2.03×10^{-17} | 0.9 | 409.3 |
| 109 | 255.82 | 26.80 | 26.23 | 2.85 | 0.36 | 2.66×10^{-17} | 0.7 | 67.8 |
| 88 | 340.75 | 7.44 | 19.33 | 4.00 | 0.37 | 8.03×10^{-17} | 0.8 | 187.5 |

Table 4
(Continued)

| Index | R.A. (deg) | Decl. (deg) | \hat{n}_S | $\hat{\gamma}$ | P_{local} | $\Phi_{90\%100\text{ TeV}}$ (TeV cm ² s) ⁻¹ | $E_{\nu,\Phi,\min}$ (TeV) | $E_{\nu,\Phi,\max}$ (TeV) |
|-------|---------------|----------------|-------------|----------------|-------------|--|------------------------------|------------------------------|
| 70 | 237.60 | 1.14 | 41.83 | 4.00 | 0.38 | 4.43×10^{-17} | 0.8 | 334.2 |
| 87 | 164.10 | -14.76 | 11.78 | 3.90 | 0.39 | 5.17×10^{-17} | 20.7 | 6368.0 |
| 46 | 105.48 | 1.66 | 25.18 | 2.74 | 0.40 | 1.73×10^{-16} | 0.8 | 320.6 |
| 102 | 343.52 | 9.69 | 42.18 | 3.38 | 0.40 | 2.69×10^{-17} | 0.7 | 158.9 |
| 66 | 354.25 | 1.40 | 27.02 | 4.00 | 0.41 | 2.40×10^{-17} | 0.8 | 338.1 |
| 92 | 144.38 | -3.14 | 18.45 | 4.00 | 0.42 | 2.90×10^{-17} | 0.9 | 517.6 |
| 100 | 128.67 | 12.76 | 5.42 | 2.18 | 0.43 | 3.28×10^{-17} | 0.7 | 123.0 |
| 110 | 143.14 | 3.32 | 21.32 | 2.82 | 0.46 | 3.36×10^{-17} | 0.8 | 281.2 |
| 97 | 228.84 | -3.96 | 6.79 | 4.00 | 0.46 | 3.30×10^{-17} | 1.0 | 620.9 |
| 91 | 304.94 | -4.97 | 12.09 | 4.00 | 0.47 | 1.34×10^{-16} | 1.1 | 871.0 |
| 63 | 264.13 | -15.07 | 8.15 | 3.88 | 0.47 | 4.46×10^{-17} | 21.1 | 6295.1 |
| 101 | 312.19 | 25.86 | 7.93 | 2.24 | 0.47 | 1.57×10^{-16} | 0.7 | 68.9 |
| 98 | 269.80 | -16.11 | 9.81 | 3.67 | 0.47 | 4.83×10^{-17} | 23.3 | 6982.3 |
| 108 | 167.45 | 12.39 | 31.98 | 3.15 | 0.48 | 5.15×10^{-17} | 0.7 | 127.1 |
| 5 | 306.96 | 19.44 | 15.41 | 2.38 | 0.49 | 4.10×10^{-17} | 0.7 | 86.9 |
| 26 | 329.57 | 1.82 | 19.70 | 4.00 | 0.49 | 1.85×10^{-17} | 0.8 | 308.3 |
| 68 | 122.25 | -0.34 | 18.24 | 3.96 | 0.51 | 2.00×10^{-17} | 0.8 | 380.2 |
| 37 | 301.20 | 10.50 | 5.10 | 2.17 | 0.51 | 3.23×10^{-17} | 0.7 | 140.9 |
| 41 | 344.50 | 1.94 | 4.08 | 2.21 | 0.52 | 2.54×10^{-17} | 0.8 | 309.0 |
| 27 | 180.72 | 3.55 | 19.65 | 3.14 | 0.55 | 2.43×10^{-17} | 0.8 | 291.7 |
| 69 | 200.71 | -31.94 | 9.69 | 3.55 | 0.57 | 2.51×10^{-17} | 61.9 | 11,967.4 |
| 117 | 5.67 | -9.06 | 7.22 | 2.95 | 0.57 | 4.89×10^{-16} | 5.5 | 2944.4 |
| 51 | 99.29 | 4.59 | 23.19 | 3.09 | 0.57 | 6.52×10^{-17} | 0.8 | 251.2 |
| 6 | 266.87 | 13.40 | 9.33 | 2.66 | 0.57 | 3.08×10^{-17} | 0.7 | 118.3 |
| 39 | 289.16 | -14.21 | 6.66 | 3.15 | 0.59 | 9.48×10^{-17} | 19.1 | 5701.6 |
| 64 | 312.60 | 59.86 | 9.68 | 2.06 | 0.59 | 8.38×10^{-17} | 0.6 | 23.8 |
| 73 | 187.17 | -6.89 | 9.57 | 2.26 | 0.61 | 4.64×10^{-17} | 1.6 | 1706.1 |
| 25 | 199.80 | 32.58 | 16.22 | 2.75 | 0.61 | 7.43×10^{-17} | 0.7 | 51.9 |
| 80 | 230.24 | 23.91 | 16.44 | 2.66 | 0.62 | 4.83×10^{-17} | 0.7 | 64.9 |
| 105 | 4.80 | -1.92 | 16.74 | 2.82 | 0.62 | 2.82×10^{-17} | 0.9 | 424.6 |
| 61 | 261.34 | -2.58 | 9.54 | 2.82 | 0.67 | 2.46×10^{-17} | 0.9 | 460.3 |
| 104 | 166.88 | -20.47 | 5.88 | 2.16 | 0.68 | 2.72×10^{-17} | 36.8 | 8851.2 |
| 22 | 37.34 | 18.88 | 27.49 | 3.83 | 0.70 | 2.80×10^{-16} | 0.7 | 101.9 |
| 32 | 169.25 | 20.84 | 22.64 | 2.87 | 0.71 | 4.67×10^{-17} | 0.7 | 79.4 |
| 107 | 233.04 | 3.02 | 35.13 | 3.54 | 0.73 | 4.45×10^{-17} | 0.8 | 281.8 |
| 118 | 263.47 | 42.52 | 6.25 | 1.99 | 0.74 | 4.06×10^{-17} | 0.7 | 40.2 |
| 58 | 193.67 | -3.81 | 6.84 | 4.00 | 0.74 | 3.21×10^{-17} | 1.0 | 588.8 |
| 20 | 266.48 | -5.10 | 9.66 | 3.55 | 0.74 | 6.92×10^{-17} | 1.1 | 948.4 |
| 116 | 30.72 | -11.91 | 6.42 | 3.38 | 0.76 | 3.81×10^{-17} | 13.6 | 4786.3 |
| 12 | 115.64 | -10.72 | 1.53 | 2.35 | 0.76 | 4.62×10^{-17} | 10.7 | 4064.4 |
| 95 | 127.53 | 35.53 | 26.45 | 2.65 | 0.77 | 9.04×10^{-17} | 0.7 | 47.3 |
| 3 | 347.90 | 22.20 | 33.17 | 4.00 | 0.79 | 8.66×10^{-17} | 0.7 | 78.2 |
| 121 | 270.36 | 25.11 | 13.05 | 4.00 | 0.79 | 4.86×10^{-17} | 0.7 | 68.2 |
| 38 | 284.97 | 19.11 | 19.88 | 4.00 | 0.80 | 3.57×10^{-16} | 0.7 | 94.0 |
| 52 | 326.72 | 27.30 | 7.78 | 2.44 | 0.80 | 4.65×10^{-17} | 0.7 | 62.8 |
| 89 | 79.63 | 8.01 | 19.75 | 4.00 | 0.81 | 4.12×10^{-17} | 0.8 | 166.7 |
| 96 | 307.97 | -32.03 | 2.48 | 2.49 | 0.81 | 3.93×10^{-17} | 61.5 | 12,416.5 |
| 47 | 110.83 | 11.45 | 4.77 | 3.57 | 0.82 | 6.09×10^{-17} | 0.7 | 136.8 |
| 57 | 103.41 | 3.96 | 2.01 | 2.14 | 0.82 | 3.55×10^{-17} | 0.8 | 281.8 |
| 62 | 79.41 | 5.00 | 12.34 | 3.04 | 0.83 | 2.81×10^{-17} | 0.8 | 260.0 |
| 42 | 293.71 | 33.32 | 7.76 | 2.89 | 0.83 | 2.83×10^{-17} | 0.7 | 48.3 |
| 82 | 4.61 | 4.36 | 16.46 | 4.00 | 0.85 | 3.26×10^{-17} | 0.8 | 272.3 |
| 19 | 194.36 | 9.59 | 25.50 | 4.00 | 0.86 | 4.15×10^{-17} | 0.7 | 158.1 |
| 103 | 225.75 | 10.77 | 12.59 | 2.88 | 0.88 | 2.55×10^{-17} | 0.7 | 141.6 |
| 36 | 33.79 | 10.09 | 2.16 | 2.01 | 0.91 | 4.01×10^{-17} | 0.8 | 158.9 |
| 76 | 310.75 | 9.07 | 9.19 | 2.17 | 0.93 | 3.58×10^{-17} | 0.7 | 165.6 |
| 21 | 222.47 | 0.89 | 17.33 | 3.34 | 0.94 | 2.55×10^{-17} | 0.8 | 342.8 |
| 67 | 214.31 | -0.89 | 8.92 | 3.32 | 0.94 | 5.71×10^{-17} | 0.8 | 363.1 |
| 71 | 193.07 | 37.50 | 14.94 | 3.19 | 0.94 | 3.45×10^{-17} | 0.7 | 42.6 |
| 17 | 314.47 | 8.39 | 30.90 | 3.32 | 0.99 | 7.36×10^{-17} | 0.8 | 171.0 |
| 111 | 96.46 | -5.08 | 0.55 | 3.35 | 1.00 | 2.74×10^{-17} | 1.1 | 924.7 |
| 53 | 327.74 | 5.82 | 1.69 | 3.75 | 1.00 | 4.50×10^{-17} | 0.8 | 229.1 |

Table 4
(Continued)

| Index | R.A. (deg) | Decl. (deg) | \hat{n}_S | $\hat{\gamma}$ | p_{local} | $\Phi_{90\%100\text{ TeV}}$ (TeV cm ² s) ⁻¹ | $E_{\nu,\Phi,\text{min}}$ (TeV) | $E_{\nu,\Phi,\text{max}}$ (TeV) |
|-------|---------------|----------------|-------------|----------------|--------------------|--|------------------------------------|------------------------------------|
| 29 | 204.43 | -2.47 | 0.00 | 2.56 | 1.00 | 1.87×10^{-17} | 0.9 | 465.6 |
| 1 | 29.32 | 1.12 | 0.00 | 2.83 | 1.00 | 1.83×10^{-17} | 0.8 | 333.4 |
| 8 | 88.31 | 0.33 | 0.00 | 3.20 | 1.00 | 2.04×10^{-17} | 0.8 | 376.7 |
| 35 | 130.01 | -10.69 | 0.00 | 1.50 | 1.00 | 5.02×10^{-17} | 10.6 | 4083.2 |

Note. The first column contains the index of the alert+ event as in Table 3. The second and third columns list the best-fit position of this work. The fourth and fifth columns contain the best-fit parameter of the likelihood optimization \hat{n}_S and $\hat{\gamma}$. The sixth column shows the local p -values, and the seventh column shows the 90% confidence level upper flux limits. The central 90% quantiles of the neutrino energies of the detected simulated events for computing the flux limit are listed in the eighth and ninth columns. They define the range in which the flux limit is valid. The global p -value for the time-integrated single-source search is 0.98.

Table 5
Results of the Time-dependent Analysis Sorted by Significance

| Index | R.A. (deg) | Decl. (deg) | \hat{n}_S | $\hat{\gamma}$ | $\hat{\mu}_T$ | $\hat{\sigma}_T$ | p_{local} |
|-------|---------------|----------------|-------------|----------------|---------------|------------------|----------------------|
| 85 | 77.43 | 5.38 | 11.98 | 2.31 | 57001 | 64 | 1.4×10^{-3} |
| 107 | 227.72 | 5.10 | 9.48 | 2.38 | 57774 | 9 | 1.6×10^{-2} |
| 17 | 318.42 | 1.75 | 10.41 | 2.45 | 57008 | 20 | 1.7×10^{-2} |
| 60 | 75.77 | 13.20 | 5.19 | 2.07 | 58155 | 10 | 1.9×10^{-2} |
| 33 | 93.74 | 14.35 | 14.45 | 2.96 | 57078 | 39 | 2.1×10^{-2} |
| 30 | 169.60 | 28.76 | 8.52 | 3.04 | 56153 | 5 | 2.5×10^{-2} |
| 83 | 21.27 | -2.95 | 18.44 | 2.90 | 57186 | 236 | 3.4×10^{-2} |
| 120 | 206.26 | 4.41 | 19.76 | 3.02 | 57427 | 103 | 5.1×10^{-2} |
| 99 | 120.19 | 5.87 | 12.71 | 2.68 | 56267 | 51 | 5.5×10^{-2} |
| 87 | 164.10 | -17.07 | 8.10 | 3.80 | 58493 | 94 | 7.3×10^{-2} |
| 47 | 24.89 | 1.56 | 11.01 | 2.70 | 57764 | 22 | 7.8×10^{-2} |
| 23 | 238.14 | 18.42 | 8.52 | 3.03 | 57173 | 5 | 8.3×10^{-2} |
| 90 | 217.59 | 0.03 | 9.40 | 2.55 | 57646 | 29 | 8.4×10^{-2} |
| 104 | 165.83 | -23.82 | 6.90 | 3.12 | 58904 | 20 | 8.6×10^{-2} |
| 11 | 307.86 | 1.36 | 3.16 | 2.04 | 57056 | 7 | 9.5×10^{-2} |
| 27 | 180.53 | 3.88 | 13.77 | 3.69 | 56470 | 26 | 9.6×10^{-2} |
| 101 | 312.19 | 26.04 | 4.81 | 2.65 | 58692 | 5 | 0.10 |
| 100 | 127.71 | 12.14 | 7.16 | 2.61 | 57214 | 5 | 0.11 |
| 44 | 350.80 | -14.90 | 5.34 | 3.08 | 57862 | 13 | 0.11 |
| 12 | 115.82 | -10.53 | 4.32 | 2.61 | 58701 | 19 | 0.11 |
| 52 | 326.72 | 27.49 | 5.81 | 1.91 | 57677 | 5 | 0.11 |
| 115 | 194.94 | 1.74 | 5.59 | 2.61 | 58529 | 6 | 0.12 |
| 6 | 266.87 | 13.40 | 6.67 | 2.39 | 55551 | 37 | 0.12 |
| 36 | 33.62 | 9.90 | 4.87 | 1.98 | 55815 | 10 | 0.12 |
| 25 | 171.74 | 26.44 | 11.23 | 2.67 | 58063 | 120 | 0.12 |
| 73 | 188.33 | -6.10 | 9.37 | 2.68 | 56698 | 78 | 0.12 |
| 16 | 68.36 | 40.82 | 3.93 | 1.66 | 58434 | 23 | 0.13 |
| 4 | 141.48 | 47.48 | 20.87 | 2.54 | 57931 | 268 | 0.13 |
| 50 | 48.32 | 0.49 | 17.16 | 3.53 | 55870 | 52 | 0.19 |
| 52 | 91.68 | 12.14 | 10.51 | 3.43 | 57694 | 12 | 0.20 |
| 2 | 298.56 | 11.55 | 8.18 | 2.67 | 56998 | 13 | 0.22 |
| 108 | 168.46 | 11.80 | 7.88 | 2.61 | 57075 | 7 | 0.23 |
| 103 | 226.14 | 10.77 | 5.93 | 2.55 | 55500 | 9 | 0.25 |
| 109 | 255.82 | 27.00 | 13.24 | 2.92 | 58940 | 32 | 0.25 |
| 28 | 70.81 | 19.08 | 8.34 | 2.85 | 58293 | 12 | 0.25 |
| 7 | 331.46 | 10.71 | 11.97 | 3.13 | 57753 | 18 | 0.26 |
| 105 | 4.80 | -0.81 | 10.26 | 2.77 | 57854 | 21 | 0.28 |
| 74 | 77.50 | 2.55 | 12.44 | 2.49 | 57407 | 144 | 0.29 |
| 34 | 224.10 | -4.09 | 5.26 | 4.00 | 56352 | 17 | 0.32 |
| 5 | 306.55 | 19.63 | 10.43 | 2.84 | 57728 | 37 | 0.33 |
| 121 | 271.00 | 25.11 | 18.65 | 4.00 | 56858 | 125 | 0.33 |
| 54 | 54.06 | 34.00 | 5.54 | 2.38 | 55465 | 8 | 0.34 |
| 78 | 227.37 | 30.25 | 7.27 | 4.00 | 56554 | 6 | 0.34 |
| 110 | 142.35 | 2.82 | 9.97 | 3.29 | 57011 | 10 | 0.34 |
| 113 | 265.01 | 5.34 | 11.57 | 2.66 | 58747 | 137 | 0.35 |

Table 5
(Continued)

| Index | R.A. (deg) | Decl. (deg) | \hat{n}_S | $\hat{\gamma}$ | $\hat{\mu}_T$ | $\hat{\sigma}_T$ | P_{local} |
|-------|---------------|----------------|-------------|----------------|---------------|------------------|-------------|
| 62 | 79.41 | 5.00 | 8.33 | 2.77 | 55881 | 23 | 0.36 |
| 51 | 100.95 | 4.98 | 13.56 | 2.74 | 57683 | 43 | 0.36 |
| 59 | 195.23 | 19.76 | 5.95 | 1.95 | 57777 | 43 | 0.37 |
| 72 | 26.38 | 9.71 | 2.64 | 1.83 | 55869 | 20 | 0.38 |
| 3 | 347.47 | 24.93 | 19.50 | 4.00 | 58817 | 67 | 0.39 |
| 40 | 193.20 | -3.22 | 4.72 | 3.27 | 56069 | 5 | 0.39 |
| 61 | 261.34 | -2.58 | 2.18 | 2.23 | 56311 | 5 | 0.40 |
| 47 | 110.83 | 11.64 | 3.10 | 2.01 | 56284 | 5 | 0.40 |
| 86 | 173.25 | -2.54 | 5.89 | 3.94 | 58914 | 8 | 0.40 |
| 31 | 353.16 | -1.40 | 4.50 | 2.61 | 57485 | 5 | 0.41 |
| 106 | 317.26 | 12.24 | 10.38 | 2.17 | 55648 | 194 | 0.42 |
| 69 | 200.71 | -31.94 | 9.17 | 2.68 | 57641 | 149 | 0.46 |
| 81 | 207.80 | 26.04 | 6.19 | 2.04 | 57909 | 35 | 0.47 |
| 8 | 88.50 | 0.46 | 3.75 | 4.00 | 58729 | 5 | 0.47 |
| 35 | 130.17 | -10.28 | 1.97 | 3.46 | 55727 | 5 | 0.48 |
| 37 | 301.37 | 10.50 | 4.16 | 2.06 | 56186 | 59 | 0.48 |
| 32 | 166.79 | 21.76 | 17.27 | 3.06 | 58039 | 105 | 0.48 |
| 26 | 329.40 | 1.12 | 10.31 | 4.00 | 57346 | 20 | 0.49 |
| 96 | 307.97 | -32.03 | 5.75 | 2.71 | 58223 | 130 | 0.49 |
| 55 | 133.55 | 27.71 | 12.73 | 4.00 | 57202 | 96 | 0.49 |
| 65 | 151.05 | 14.93 | 10.71 | 2.69 | 56073 | 74 | 0.50 |
| 102 | 341.35 | 11.01 | 23.55 | 3.50 | 55932 | 225 | 0.50 |
| 53 | 327.92 | 5.82 | 7.41 | 3.54 | 57307 | 5 | 0.51 |
| 10 | 284.83 | 3.32 | 2.92 | 1.95 | 58860 | 51 | 0.52 |
| 1 | 29.51 | 1.23 | 4.52 | 4.00 | 58152 | 5 | 0.52 |
| 97 | 228.25 | -4.44 | 4.67 | 4.00 | 57925 | 23 | 0.54 |
| 18 | 9.38 | 7.59 | 2.45 | 1.76 | 56920 | 133 | 0.55 |
| 114 | 105.55 | 6.38 | 10.56 | 3.26 | 57438 | 73 | 0.55 |
| 98 | 268.20 | -16.29 | 8.79 | 3.93 | 55171 | 32 | 0.56 |
| 75 | 47.55 | 15.44 | 6.99 | 2.85 | 56015 | 6 | 0.56 |
| 19 | 199.21 | 8.87 | 9.84 | 3.33 | 58512 | 16 | 0.58 |
| 21 | 223.65 | 1.67 | 6.06 | 2.04 | 57754 | 58 | 0.59 |
| 46 | 105.67 | 0.97 | 8.75 | 2.52 | 56044 | 62 | 0.60 |
| 49 | 168.88 | -1.43 | 12.14 | 4.00 | 57034 | 135 | 0.60 |
| 88 | 340.60 | 7.59 | 6.69 | 4.00 | 56225 | 10 | 0.63 |
| 122 | 60.12 | -3.99 | 4.24 | 4.00 | 57539 | 33 | 0.64 |
| 20 | 266.67 | -5.10 | 9.44 | 3.81 | 57444 | 122 | 0.65 |
| 79 | 282.81 | 8.26 | 16.67 | 2.98 | 57871 | 144 | 0.66 |
| 92 | 144.78 | -2.95 | 12.23 | 4.00 | 58406 | 95 | 0.67 |
| 91 | 307.53 | -4.97 | 6.03 | 2.39 | 57105 | 26 | 0.68 |
| 95 | 130.33 | 36.92 | 10.91 | 4.00 | 55469 | 51 | 0.68 |
| 82 | 359.34 | 4.36 | 11.18 | 3.54 | 56650 | 26 | 0.68 |
| 80 | 230.45 | 23.54 | 8.44 | 2.91 | 56927 | 13 | 0.68 |
| 112 | 29.00 | 3.47 | 3.64 | 4.00 | 57045 | 5 | 0.69 |
| 93 | 270.56 | -7.29 | 6.61 | 2.10 | 58532 | 44 | 0.69 |
| 70 | 237.20 | 1.14 | 16.00 | 3.27 | 56123 | 65 | 0.70 |
| 22 | 37.14 | 18.69 | 16.67 | 2.89 | 57494 | 112 | 0.73 |
| 66 | 354.64 | 1.73 | 4.05 | 2.30 | 57815 | 5 | 0.73 |
| 119 | 207.07 | 13.27 | 6.99 | 3.26 | 56078 | 20 | 0.74 |
| 25 | 199.80 | 32.58 | 6.94 | 2.41 | 55763 | 38 | 0.74 |
| 39 | 289.35 | -15.33 | 3.13 | 3.60 | 58116 | 8 | 0.75 |
| 63 | 263.76 | -15.07 | 5.68 | 3.72 | 57964 | 136 | 0.76 |
| 15 | 272.55 | 36.20 | 5.39 | 1.97 | 55850 | 40 | 0.76 |
| 57 | 102.85 | 3.77 | 5.77 | 4.00 | 57412 | 5 | 0.77 |
| 77 | 97.34 | -15.06 | 2.86 | 3.94 | 57966 | 5 | 0.79 |
| 111 | 96.46 | -5.08 | 3.54 | 3.78 | 55790 | 14 | 0.80 |
| 117 | 6.66 | -9.98 | 9.12 | 3.27 | 55227 | 69 | 0.82 |
| 94 | 25.91 | 7.61 | 24.88 | 3.40 | 56859 | 99 | 0.82 |
| 84 | 39.94 | 13.64 | 23.44 | 4.00 | 58516 | 221 | 0.83 |
| 14 | 235.34 | 19.76 | 10.65 | 2.42 | 58482 | 76 | 0.84 |
| 58 | 194.20 | -3.81 | 6.96 | 2.76 | 55443 | 224 | 0.84 |
| 89 | 77.12 | 7.68 | 4.52 | 4.00 | 57329 | 5 | 0.84 |
| 76 | 310.55 | 6.39 | 9.45 | 2.80 | 55956 | 23 | 0.85 |

Table 5
(Continued)









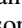




















| Index | R.A. (deg) | Decl. (deg) | \hat{n}_s | $\hat{\gamma}$ | $\hat{\mu}_T$ | $\hat{\sigma}_T$ | P_{local} |
|-------|---------------|----------------|-------------|----------------|---------------|------------------|-------------|
| 67 | 214.12 | -0.71 | 6.49 | 3.58 | 57509 | 22 | 0.87 |
| 29 | 205.30 | -2.65 | 6.59 | 3.19 | 56484 | 7 | 0.87 |
| 64 | 312.23 | 60.79 | 5.30 | 2.32 | 56903 | 7 | 0.88 |
| 13 | 137.87 | -2.87 | 20.28 | 3.26 | 57963 | 386 | 0.90 |
| 9 | 111.16 | -0.21 | 6.61 | 2.97 | 58059 | 19 | 0.90 |
| 68 | 122.43 | -1.08 | 9.92 | 3.52 | 55389 | 127 | 0.91 |
| 56 | 280.64 | 30.35 | 12.20 | 2.57 | 57865 | 153 | 0.91 |
| 116 | 30.54 | -11.15 | 3.03 | 2.49 | 57403 | 5 | 0.93 |
| 41 | 345.19 | 1.40 | 8.92 | 3.69 | 55980 | 35 | 0.93 |
| 42 | 293.51 | 33.32 | 4.21 | 4.00 | 56102 | 5 | 0.94 |
| 38 | 287.16 | 19.47 | 10.07 | 4.00 | 55637 | 45 | 0.96 |
| 45 | 346.71 | 18.24 | 12.32 | 2.61 | 55259 | 143 | 0.97 |
| 118 | 263.21 | 42.52 | 6.51 | 3.44 | 56064 | 6 | 0.98 |
| 71 | 191.42 | 35.21 | 4.87 | 1.60 | 55301 | 42 | 0.99 |

Note. The first column contains the alert+ index as in Table 3. The second and third columns list the best-fit position. The fourth and fifth columns contain the best-fit parameter of the likelihood optimizations n_s and γ . The sixth and seventh columns list the best-fit results for the Gaussian time window with mean μ_T and width σ_T . The eighth column shows the local p -values. The global p -value for the time-dependent analysis is 0.156.

ORCID iDs

- R. Abbasi <https://orcid.org/0000-0001-6141-4205>
M. Ackermann <https://orcid.org/0000-0001-8952-588X>
S. K. Agarwalla <https://orcid.org/0000-0002-9714-8866>
J. A. Aguilar <https://orcid.org/0000-0003-2252-9514>
M. Ahlers <https://orcid.org/0000-0003-0709-5631>
J. M. Alameddine <https://orcid.org/0000-0002-9534-9189>
K. Andeen <https://orcid.org/0000-0001-9394-0007>
G. Anton <https://orcid.org/0000-0003-2039-4724>
C. Argüelles <https://orcid.org/0000-0003-4186-4182>
S. N. Axani <https://orcid.org/0000-0001-8866-3826>
X. Bai <https://orcid.org/0000-0002-1827-9121>
A. Balagopal V. <https://orcid.org/0000-0001-5367-8876>
S. W. Barwick <https://orcid.org/0000-0003-2050-6714>
V. Basu <https://orcid.org/0000-0002-9528-2009>
J. J. Beatty <https://orcid.org/0000-0003-0481-4952>
J. Becker Tjus <https://orcid.org/0000-0002-1748-7367>
J. Beise <https://orcid.org/0000-0002-7448-4189>
C. Bellenghi <https://orcid.org/0000-0001-8525-7515>
S. BenZvi <https://orcid.org/0000-0001-5537-4710>
E. Bernardini <https://orcid.org/0000-0003-3108-1141>
D. Z. Besson <https://orcid.org/0000-0001-6733-963X>
E. Blaufuss <https://orcid.org/0000-0001-5450-1757>
S. Blot <https://orcid.org/0000-0003-1089-3001>
J. Y. Book <https://orcid.org/0000-0001-6687-5959>
C. Boscolo Meneguolo <https://orcid.org/0000-0001-8325-4329>
S. Böser <https://orcid.org/0000-0002-5918-4890>
O. Botner <https://orcid.org/0000-0001-8588-7306>
J. Böttcher <https://orcid.org/0000-0002-3387-4236>
B. Brinson <https://orcid.org/0000-0001-9128-1159>
M. A. Campana <https://orcid.org/0000-0003-4162-5739>
C. Chen <https://orcid.org/0000-0002-8139-4106>
Z. Chen <https://orcid.org/0000-0002-2813-7688>
D. Chirkin <https://orcid.org/0000-0003-4911-1345>
B. A. Clark <https://orcid.org/0000-0003-4089-2245>
A. Coleman <https://orcid.org/0000-0003-1510-1712>
J. M. Conrad <https://orcid.org/0000-0002-6393-0438>
P. Coppin <https://orcid.org/0000-0001-6869-1280>
P. Correa <https://orcid.org/0000-0002-1158-6735>
D. F. Cowen <https://orcid.org/0000-0003-4738-0787>
P. Dave <https://orcid.org/0000-0002-3879-5115>
C. De Clercq <https://orcid.org/0000-0001-5266-7059>
J. J. DeLaunay <https://orcid.org/0000-0001-5229-1995>
D. Delgado <https://orcid.org/0000-0002-4306-8828>
A. Desai <https://orcid.org/0000-0001-7405-9994>
P. Desiati <https://orcid.org/0000-0001-9768-1858>
K. D. de Vries <https://orcid.org/0000-0002-9842-4068>
G. de Wasseige <https://orcid.org/0000-0002-1010-5100>
T. DeYoung <https://orcid.org/0000-0003-4873-3783>
A. Diaz <https://orcid.org/0000-0001-7206-8336>
J. C. Díaz-Vélez <https://orcid.org/0000-0002-0087-0693>
H. Dujmovic <https://orcid.org/0000-0003-1891-0718>
M. A. DuVernois <https://orcid.org/0000-0002-2987-9691>
P. Eller <https://orcid.org/0000-0001-6354-5209>
D. Elsässer <https://orcid.org/0000-0001-6796-3205>
H. Erpenbeck <https://orcid.org/0000-0001-6319-2108>
P. A. Evenson <https://orcid.org/0000-0001-7929-810X>
K. L. Fan <https://orcid.org/0000-0002-8246-4751>
A. R. Fazely <https://orcid.org/0000-0002-6907-8020>
A. Fedynitch <https://orcid.org/0000-0003-2837-3477>
C. Finley <https://orcid.org/0000-0003-3350-390X>
L. Fischer <https://orcid.org/0000-0002-7645-8048>
D. Fox <https://orcid.org/0000-0002-3714-672X>
A. Franckowiak <https://orcid.org/0000-0002-5605-2219>
E. Ganster <https://orcid.org/0000-0003-4393-6944>
A. Garcia <https://orcid.org/0000-0002-8186-2459>
A. Ghadimi <https://orcid.org/0000-0002-6350-6485>
C. Glaser <https://orcid.org/0000-0001-5998-2553>
T. Glauch <https://orcid.org/0000-0003-1804-4055>
T. Glüsenskamp <https://orcid.org/0000-0002-2268-9297>
S. Goswami <https://orcid.org/0000-0002-0373-9770>
S. J. Gray <https://orcid.org/0000-0003-2907-8306>
S. Griffin <https://orcid.org/0000-0002-0779-9623>

- S. Griswold <https://orcid.org/0000-0002-7321-7513>
 K. M. Groth <https://orcid.org/0000-0002-1581-9049>
 P. Gutjahr <https://orcid.org/0000-0001-7980-7285>
 A. Hallgren <https://orcid.org/0000-0001-7751-4489>
 L. Halve <https://orcid.org/0000-0003-2237-6714>
 F. Halzen <https://orcid.org/0000-0001-6224-2417>
 H. Hamdaoui <https://orcid.org/0000-0001-5709-2100>
 A. Haungs <https://orcid.org/0000-0002-9638-7574>
 K. Helbing <https://orcid.org/0000-0003-2072-4172>
 F. Henningsen <https://orcid.org/0000-0002-0680-6588>
 N. Heyer <https://orcid.org/0000-0001-9036-8623>
 C. Hill <https://orcid.org/0000-0003-0647-9174>
 W. Hou <https://orcid.org/0000-0003-3422-7185>
 T. Huber <https://orcid.org/0000-0002-6515-1673>
 K. Hultqvist <https://orcid.org/0000-0003-0602-9472>
 M. Hünnefeld <https://orcid.org/0000-0002-2827-6522>
 G. S. Japaridze <https://orcid.org/0000-0002-7000-5291>
 M. Jeong <https://orcid.org/0000-0003-2420-6639>
 M. Jin <https://orcid.org/0000-0003-0487-5595>
 B. J. P. Jones <https://orcid.org/0000-0003-3400-8986>
 D. Kang <https://orcid.org/0000-0002-5149-9767>
 W. Kang <https://orcid.org/0000-0003-3980-3778>
 A. Kappes <https://orcid.org/0000-0003-1315-3711>
 T. Karg <https://orcid.org/0000-0003-3251-2126>
 M. Karl <https://orcid.org/0000-0003-2475-8951>
 A. Karle <https://orcid.org/0000-0001-9889-5161>
 U. Katz <https://orcid.org/0000-0002-7063-4418>
 M. Kauer <https://orcid.org/0000-0003-1830-9076>
 J. L. Kelley <https://orcid.org/0000-0002-0846-4542>
 A. Khatee Zathul <https://orcid.org/0000-0002-8735-8579>
 A. Kheirandish <https://orcid.org/0000-0001-7074-0539>
 J. Kiryluk <https://orcid.org/0000-0003-0264-3133>
 S. R. Klein <https://orcid.org/0000-0003-2841-6553>
 A. Kochocki <https://orcid.org/0000-0003-3782-0128>
 R. Koirala <https://orcid.org/0000-0002-7735-7169>
 H. Kolanoski <https://orcid.org/0000-0003-0435-2524>
 T. Kontrimas <https://orcid.org/0000-0001-8585-0933>
 L. Köpke <https://orcid.org/0000-0001-8530-6348>
 C. Kopper <https://orcid.org/0000-0001-6288-7637>
 D. J. Koskinen <https://orcid.org/0000-0002-0514-5917>
 P. Koundal <https://orcid.org/0000-0002-5917-5230>
 M. Kovacevich <https://orcid.org/0000-0002-5019-5745>
 M. Kowalski <https://orcid.org/0000-0001-8594-8666>
 J. Krishnamoorthi <https://orcid.org/0009-0006-1352-2248>
 A. Kumar <https://orcid.org/0000-0002-8367-8401>
 N. Kurahashi <https://orcid.org/0000-0003-1047-8094>
 N. Lad <https://orcid.org/0000-0001-9302-5140>
 C. Lagunas Gualda <https://orcid.org/0000-0002-9040-7191>
 M. Lamoureux <https://orcid.org/0000-0002-8860-5826>
 M. J. Larson <https://orcid.org/0000-0002-6996-1155>
 F. Lauber <https://orcid.org/0000-0001-5648-5930>
 J. P. Lazar <https://orcid.org/0000-0003-0928-5025>
 J. W. Lee <https://orcid.org/0000-0001-5681-4941>
 K. Leonard DeHolton <https://orcid.org/0000-0002-8795-0601>
 A. Leszczyńska <https://orcid.org/0000-0003-0935-6313>
 M. Lincetto <https://orcid.org/0000-0002-1460-3369>
 Q. R. Liu <https://orcid.org/0000-0003-3379-6423>
 E. Lohfink <https://orcid.org/0000-0003-3248-5682>
 L. Lu <https://orcid.org/0000-0003-3175-7770>
 F. Lucarelli <https://orcid.org/0000-0002-9558-8788>
 W. Luszczak <https://orcid.org/0000-0003-3085-0674>
 Y. Lyu <https://orcid.org/0000-0002-2333-4383>
 J. Madsen <https://orcid.org/0000-0003-2415-9959>
 E. Manao <https://orcid.org/0009-0002-6197-8574>
 I. C. Mariş <https://orcid.org/0000-0002-5771-1124>
 R. Maruyama <https://orcid.org/0000-0003-2794-512X>
 F. Mayhew <https://orcid.org/0000-0001-7609-403X>
 F. McNally <https://orcid.org/0000-0002-0785-2244>
 K. Meagher <https://orcid.org/0000-0003-3967-1533>
 M. Meier <https://orcid.org/0000-0002-9483-9450>
 L. Merten <https://orcid.org/0000-0003-1332-9895>
 T. Montaruli <https://orcid.org/0000-0001-5014-2152>
 R. W. Moore <https://orcid.org/0000-0003-4160-4700>
 M. Moulai <https://orcid.org/0000-0001-7909-5812>
 R. Naab <https://orcid.org/0000-0003-2512-466X>
 R. Nagai <https://orcid.org/0000-0001-7503-2777>
 J. Necker <https://orcid.org/0000-0003-0280-7484>
 H. Niederhausen <https://orcid.org/0000-0002-9566-4904>
 M. U. Nisa <https://orcid.org/0000-0002-6859-3944>
 S. C. Nowicki <https://orcid.org/0000-0003-2497-8057>
 A. Obertacke Pollmann <https://orcid.org/0000-0002-2492-043X>
 B. Oeyen <https://orcid.org/0000-0003-2940-3164>
 E. O'Sullivan <https://orcid.org/0000-0003-1882-8802>
 H. Pandya <https://orcid.org/0000-0002-6138-4808>
 N. Park <https://orcid.org/0000-0002-4282-736X>
 E. N. Paudel <https://orcid.org/0000-0001-9276-7994>
 C. Pérez de los Heros <https://orcid.org/0000-0002-2084-5866>
 J. Peterson <https://orcid.org/0000-0002-7985-1443>
 S. Philippen <https://orcid.org/0000-0002-0276-0092>
 A. Pizzuto <https://orcid.org/0000-0002-8466-8168>
 M. Plum <https://orcid.org/0000-0001-8691-242X>
 B. Pries <https://orcid.org/0000-0003-4811-9863>
 C. Raab <https://orcid.org/0000-0001-9921-2668>
 A. Rehman <https://orcid.org/0000-0001-7616-5790>
 E. Resconi <https://orcid.org/0000-0003-0705-2770>
 S. Reusch <https://orcid.org/0000-0002-7788-628X>
 W. Rhode <https://orcid.org/0000-0003-2636-5000>
 B. Riedel <https://orcid.org/0000-0002-9524-8943>
 M. Rongen <https://orcid.org/0000-0002-7057-1007>
 C. Rott <https://orcid.org/0000-0002-6958-6033>
 T. Ruhe <https://orcid.org/0000-0002-4080-9563>
 D. Ryckbosch <https://orcid.org/0000-0002-8759-7553>
 I. Safa <https://orcid.org/0000-0001-8737-6825>
 D. Salazar-Gallegos <https://orcid.org/0000-0002-9312-9684>
 A. Sandrock <https://orcid.org/0000-0002-6779-1172>
 M. Santander <https://orcid.org/0000-0001-7297-8217>
 S. Sarkar <https://orcid.org/0000-0002-1206-4330>
 S. Sarkar <https://orcid.org/0000-0002-3542-858X>
 H. Schieler <https://orcid.org/0000-0002-2637-4778>
 S. Schindler <https://orcid.org/0000-0001-5507-8890>
 L. Schlickmann <https://orcid.org/0000-0002-9746-6872>
 F. Schlüter <https://orcid.org/0000-0002-5545-4363>
 J. Schneider <https://orcid.org/0000-0001-7752-5700>
 F. G. Schröder <https://orcid.org/0000-0001-8495-7210>
 L. Schumacher <https://orcid.org/0000-0001-8945-6722>
 S. Sclafani <https://orcid.org/0000-0001-9446-1219>
 S. Seunarine <https://orcid.org/0000-0003-3272-6896>
 M. Silva <https://orcid.org/0000-0001-6940-8184>
 B. Skrzypek <https://orcid.org/0000-0002-0910-1057>
 B. Smithers <https://orcid.org/0000-0003-1273-985X>
 J. Soedingrekso <https://orcid.org/0000-0003-1011-2797>

D. Soldin  <https://orcid.org/0000-0003-3005-7879>
 G. Sommani  <https://orcid.org/0000-0002-0094-826X>
 G. M. Spiczak  <https://orcid.org/0000-0002-0030-0519>
 C. Spiering  <https://orcid.org/0000-0001-7372-0074>
 T. Stezelberger  <https://orcid.org/0000-0003-2676-9574>
 T. Stuttard  <https://orcid.org/0000-0001-7944-279X>
 G. W. Sullivan  <https://orcid.org/0000-0002-2585-2352>
 I. Taboada  <https://orcid.org/0000-0003-3509-3457>
 S. Ter-Antonyan  <https://orcid.org/0000-0002-5788-1369>
 W. G. Thompson  <https://orcid.org/0000-0003-2988-7998>
 J. Thwaites  <https://orcid.org/0000-0001-9179-3760>
 K. Tollefson  <https://orcid.org/0000-0001-9725-1479>
 S. Toscano  <https://orcid.org/0000-0002-1860-2240>
 A. Trettin  <https://orcid.org/0000-0003-0350-3597>
 C. F. Tung  <https://orcid.org/0000-0001-6920-7841>
 M. A. Unland Elorrieta  <https://orcid.org/0000-0002-6124-3255>
 A. K. Upadhyay  <https://orcid.org/0000-0003-1957-2626>
 N. Valtonen-Mattila  <https://orcid.org/0000-0002-1830-098X>
 J. Vandenbroucke  <https://orcid.org/0000-0002-9867-6548>
 N. van Eijndhoven  <https://orcid.org/0000-0001-5558-3328>
 J. van Santen  <https://orcid.org/0000-0002-2412-9728>
 S. Verpoest  <https://orcid.org/0000-0002-3031-3206>
 C. Walck  <https://orcid.org/0000-0002-4188-9219>
 C. Weaver  <https://orcid.org/0000-0003-2385-2559>
 J. Weldert  <https://orcid.org/0000-0002-3709-2354>
 C. Wendt  <https://orcid.org/0000-0001-8076-8877>
 N. Whitehorn  <https://orcid.org/0000-0002-3157-0407>
 C. H. Wiebusch  <https://orcid.org/0000-0002-6418-3008>
 M. Wolf  <https://orcid.org/0000-0001-9991-3923>
 S. Yoshida  <https://orcid.org/0000-0003-2480-5105>
 T. Yuan  <https://orcid.org/0000-0002-7041-5872>
 Z. Zhang  <https://orcid.org/0000-0002-7347-283X>

References

- Aartsen, M., Ackermann, M., Adams, J., et al. 2020, *JInst*, 15, P06032
 Aartsen, M. G., Ackermann, M., Adams, J., et al. 2015, *ApJ*, 807, 46
 Aartsen, M. G., Ackermann, M., Adams, J., et al. 2017a, *JInst*, 12, P03012
 Aartsen, M. G., Ackermann, M., Adams, J., et al. 2017b, *Aph*, 92, 30
 Aartsen, M. G., Ackermann, M., Adams, J., et al. 2020, *PhRvL*, 124, 051103
 Aartsen, M. G., Ackermann, M., Adams, J., et al. 2018a, *Sci*, 361, 378
 Aartsen, M. G., Ackermann, M., Adams, J., et al. 2018b, *Sci*, 361, 147
 Abbasi, R., Abdou, Y., Abu-Zayyad, T., et al. 2011, *ApJ*, 732, 18
 Abbasi, R., Ackermann, M., Adams, J., et al. 2021a, *PhRvD*, 104, 022002
 Abbasi, R., Ackermann, M., Adams, J., et al. 2021b, arXiv:2101.09836
 Abbasi, R., Ackermann, M., Adams, J., et al. 2021c, *ApJL*, 920, L45
 Abbasi, R., Ackermann, M., Adams, J., et al. 2022a, *Sci*, 378, 538
 Abbasi, R., Ackermann, M., Adams, J., et al. 2022b, *ApJ*, 928, 50
 Abbasi, R., Ackermann, M., Adams, J., et al. 2023a, *ApJS*, 269, 25
 Abbasi, R., Ackermann, M., Adams, J., et al. 2023b, *ApJ*, 951, 45
 Abbasi, R., Ackermann, M., Adams, J., et al. 2021d, *ApJ*, 911, 67
 Abdo, A. A., Ackermann, M., Ajello, M., et al. 2010, *ApJS*, 188, 405
 Acero, F., Ackermann, M., Ajello, M., et al. 2015, *ApJS*, 218, 23
 Ackermann, M., Ajello, M., Albert, A., et al. 2012, *ApJS*, 203, 4
 Bartoli, B., Bernardini, P., Bi, X. J., et al. 2013, *A&A*, 551, A142
 Bianchi, L., Efremova, B., Herald, J., et al. 2011, *MNRAS*, 411, 2770
 Blaufuss, E., Kintscher, T., Lu, L., & Tung, C. F. 2019, *ICRC (Madison, WI)*, 358, 1021
 Boller, T., Freyberg, M. J., Trümper, J., et al. 2016, *A&A*, 588, A103
 Braun, J., Baker, M., Dumm, J., et al. 2010, *Aph*, 33, 175
 Braun, J., Dumm, J., De Palma, F., et al. 2008, *Aph*, 29, 299
 Condon, J. J., Cotton, W. D., Greisen, E. W., et al. 1998, *AJ*, 115, 1693
 D'Elia, V., Perri, M., Puccetti, S., et al. 2013, *A&A*, 551, A142
 Dempster, A. P., Laird, N. M., & Rubin, D. B. 1977, *J. R. Stat. Soc. Ser. B Methodol.*, 39, 1
 Eller, P., & Shtembari, L. 2023, *JInst*, 18, P03048
 Evans, P. A., Osborne, J. P., Beardmore, A. P., et al. 2014, *ApJS*, 210, 8
 Giommi, P., Arrigo, G., Barres De Almeida, U., et al. 2018, arXiv:1805.08505
 Gregory, P. C., Scott, W. K., Douglas, K., & Condon, J. J. 1996, *ApJS*, 103, 427
 Haack, C., & Wiebusch, C. 2017, *ICRC (Busan)*, 301, 1005
 Healey, S. E., Romani, R. W., Taylor, G. B., et al. 2007, *ApJS*, 171, 61
 Jackson, N., Battye, R. A., Browne, I. W. A., et al. 2007, *MNRAS*, 376, 371
 Karl, M. 2019, *ICRC (Madison, WI)*, 36, 929
 Karl, M., Abbasi, R., Ackermann, M., et al. 2023, *ICRC (Nagoya)*, 444, 974
 Karl, M., & Eller, P. 2023, arXiv:2312.15196
 Karl, M., Eller, P., & Schubert, A. 2021, *ICRC (Berlin)*, 37, 940
 Karl, M. S. 2022, Dissertation, Technische Univ. München, München <https://mediatum.ub.tum.de/node?id=1654955>
 Kintscher, T. 2016, *JPhCS*, 718, 062029
 Kronmueller, M., & Glauch, T. 2019, *ICRC (Madison, WI)*, 36, 937
 Myers, S. T., Jackson, N. J., Browne, I. W. A., et al. 2003, *MNRAS*, 341, 1
 Nieppola, E., Tornikoski, M., Lähteenmäki, A., et al. 2007, *AJ*, 133, 1947
 Nolan, P. L., Abdo, A. A., Ackermann, M., et al. 2012, *ApJS*, 199, 31
 Padovani, P., Giommi, P., Falomo, R., et al. 2022, *MNRAS*, 510, 2671
 Planck Collaboration, Ade, P. A. R., Aghanim, N., et al. 2011, *A&A*, 536, A7
 Planck Collaboration, Ade, P. A. R., Aghanim, N., et al. 2014, *A&A*, 571, A28
 Planck Collaboration, Ade, P. A. R., Aghanim, N., et al. 2016, *A&A*, 594, A26
 Voges, W., Aschenbach, B., Boller, T., et al. 1999, *A&A*, 349, 389
 Waxman, E., & Bahcall, J. N. 1999, *PhRvD*, 59, 023002
 White, R. L., & Becker, R. H. 1992, *ApJS*, 79, 331
 Wilks, S. S. 1938, *Ann. Math. Stat.*, 9, 60
 Wright, A. E., Griffith, M. R., Burke, B. F., & Ekers, R. D. 1994, *ApJS*, 91, 111
 Wright, E. L., Eisenhardt, P. R. M., Mainzer, A. K., et al. 2010, *AJ*, 140, 1868